THz-frequency magnon-phonon-polaritons in the collective strong-coupling regime Ⓕ

Prasahnt Sivarajah ⓘD, Andreas Steinbacher ⓘD, Blake Dastrup, Jian Lu ⓘD, Maolin Xiang, Wei Ren, Stanislav Kamba ⓘD, Shixun Cao ⓘD, and Keith A. Nelson ⓘD

COLLECTIONS

Note: This paper is part of the Special Topic section "Advances in Terahertz Solid-State Physics and Devices" published in J. Appl. Phys. 125(15) (2019).

Ⓕ This paper was selected as Featured

View Online   Export Citation   CrossMark

THz-frequency magnon-phonon-polaritons in the collective strong-coupling regime Ⓕ

Prasahnt Sivarajah,[1] Ⓘ Andreas Steinbacher,[1] Ⓘ Blake Dastrup,[1] Jian Lu,[1] Ⓘ Maolin Xiang,[2] Wei Ren,[2]
Stanislav Kamba,[3] Ⓘ Shixun Cao,[2] Ⓘ and Keith A. Nelson[1,a) Ⓘ

AFFILIATIONS

[1]Department of Chemistry, Massachusetts Institute of Technology, Cambridge, Massachusetts 02139, USA
[2]Department of Physics, International Center of Quantum and Molecular Structures and Materials Genome Institute,
Shanghai University, Shanghai 200444, China
[3]Institute of Physics, Academy of Sciences of the Czech Republic, Na Slovance 2, 182 21 Prague 8, Czech Republic

ABSTRACT

Strong coupling between light and matter occurs when the two interact such that new hybrid modes, the so-called polaritons, are formed. Here, we report on the strong coupling of both the electric and the magnetic degrees of freedom to an ultrafast terahertz (THz) frequency electromagnetic wave. In our system, optical phonons in a slab of ferroelectric lithium niobate are strongly coupled to a THz electric field to form phonon-polaritons, which are simultaneously strongly coupled to magnons in an adjacent slab of canted antiferromagnetic erbium orthoferrite via the magnetic-field component of the same THz pulse. We juxtapose experimental results of bare slabs consisting of the two materials with a photonic crystal cavity, consisting of a two-dimensional array of air holes cut into the hybrid slab. In both cases, the strong coupling leads to the formation of new magnon-phonon-polariton modes, which we experimentally observe in the time domain as a normal-mode beating and which corresponds in the frequency domain to an avoided crossing. Our simple yet versatile waveguide platform provides a promising avenue through which to explore ultrafast THz spintronics, quantum electrodynamics, sensing, and spectroscopic applications.

I. INTRODUCTION

The interaction between an electromagnetic wave (light) and an atomic, a molecular, or a material mode is termed "strong coupling" if the rate of coherent energy transfer between the light and matter is faster than the irreversible decay of the light or the coherent material excitation. In the strong-coupling regime, the electromagnetic and material modes can no longer be treated as separate entities but rather form two hybrid modes called polaritons, with an energy difference between the modes given by the splitting energy $\hbar\Omega$.[1–4] Polariton systems enable extensive optical control over material behavior and coherent information transfer between light and material degrees of freedom at a rate Ω, yielding opportunities for both classical[5,6] and quantum information processing.[7–9] Earlier, the strong coupling of the electric field of

light to the electric dipole moments of atoms was explored,[10] and later, it was also demonstrated with superconducting qubits and excitons.[11–15] More recently, coupling to magnetic moments has been studied using magnetically active systems such as nitrogen-vacancy (NV) centers and magnon spin waves.[16–18] Cavity-enhanced versions of this coupling have also been observed, for example, between photons and a diverse range of excitations, including (Rydberg) atom transitions,[19–21] excitons,[22] plasmons,[23] NV center spins,[24] magnons,[25] two-dimensional electron gases,[26] and Cooper pairs of a superconductor.[11] A subset of demonstrations has even reached the single-photon or few-photon level, which falls under the field of cavity quantum electrodynamics (QED).[8,9] While quantum demonstrations motivate cutting-edge applications such as quantum computation[27]—for which dispersive

coupling between a cavity and a two-level system might be used for repeated measurements of a qubit via a quantum nondemolition method[28,29]—strong coupling can also be based on the classical coherence of macroscopic electrodynamic fields. The latter not only serves as important groundwork for its quantum analogs, but also has applications of its own right in fields such as lasing[11,12] and sensing.[13,14]

Spintronics, in its quest toward long-range and high-bandwidth operation, would particularly benefit from such strong coupling because light can provide a means for facile transport and interaction with spin information. Moreover, cavity-enhanced versions of this coupling can be used to achieve long-term storage and all-optical addressing of spin states, important elements in realizing spin-based computation. Many of these possibilities already exist in the microwave frequency range. For example, in recent advances, magnons have been used as data carriers,[30,31] because, unlike spin-polarized electrons, they provide transfer of spin information over macroscopic distances without any Joule heating and enable access to wave-based computing concepts. Meanwhile, the first classical demonstration of cavity spintronics was reported by Zhang *et al.* using microwave cavity photons and magnons in yttrium iron garnet (YIG).[18] They observed a Rabi-like oscillation of the light intensity, which they attributed to the coupling between the magnetic field of the EM wave and the magnetization of YIG.

The first report of polaritons formed by the strong coupling of terahertz (THz) light and magnons was by Sanders *et al.* in 1978,[32] wherein a slab of iron (II) fluoride that exhibits an antiferromagnetic resonance at 1.58 THz was used. More recently, Kampfrath *et al.* used advancements in the generation of ultrashort THz pulses to demonstrate control over the coherent superposition of antiferromagnetic magnons in nickel oxide.[33] There have also been demonstrations at THz frequencies of the inverse Faraday effect[34] and nonlinear spin control.[35–37] The prospect of harnessing these properties makes it desirable to realize a magnon-based spintronics platform at THz frequencies, but this has been difficult to achieve due to a scarcity of appropriate sources and detectors. Optical light can be used for generation and detection of THz magnons, but the interaction is either indirect[38,39] or nonlinear[40] and the efficiency is not high. Meanwhile, free-space THz light has been shown to exert direct linear control over magnons[33,41] but is not conducive to realizing miniaturized devices. Moreover, a cavity-enhanced version of this platform has been elusive due to the added constraint of requiring a highly confining THz cavity.

Here, we overcome these limitations using the THz polaritonics on-chip waveguide platform to demonstrate collective strong coupling of both magnons and phonons to THz light, with and without the utilization of a cavity structure. This platform has already been utilized to demonstrate capabilities such as spatiotemporal coherent control of lattice vibrational waves,[42] time-resolved near-field THz imaging,[43] and on-chip all-dielectric devices.[44] Its great advantages are the high confinement and the efficient all-optical generation and detection of the polaritons on subcycle time scales and subwavelength length scales. Using this platform, optical phonons in a slab of ferroelectric lithium niobate (LiNbO$_3$, LN) are strongly coupled to a THz electric field to form phonon-polaritons, which are simultaneously strongly coupled to magnons in an adjacent slab of canted antiferromagnetic erbium orthoferrite (ErFeO$_3$, EFO) via the THz magnetic field. In addition, we also confine the THz waves in a photonic crystal cavity fabricated by patterning the hybrid LN–EFO slab with a two-dimensional array of air holes. In both patterned and unpatterned hybrid waveguide samples, the strong coupling leads to the formation of new modes we term magnon-phonon-polaritons, which we experimentally observe in the time domain as beating between the upper and lower polariton branch modes, corresponding in the frequency domain to avoided crossings. Coupling to the magnons in EFO forms the basis for a spintronic platform, while coupling to the phonons in LN enables the efficient generation and detection of light directly inside the cavity. Our simple yet versatile waveguide platform, thus, provides a promising avenue through which to explore ultrafast THz spintronics, quantum electrodynamics, sensing, and spectroscopic applications.

II. GENERATION AND DETECTION OF MAGNON-PHONON-POLARITONS

A. Sample structures

The four different sample structures under investigation are sketched in Fig. 1. For all samples, we started with a 53 μm thick (100) LN MgO-doped stoichiometric melt single crystal grown by the Czochralski method and diced to dimensions of 11 × 10 mm². For the hybrid waveguide/cavity [see Figs. 1(b) and 1(d)], an
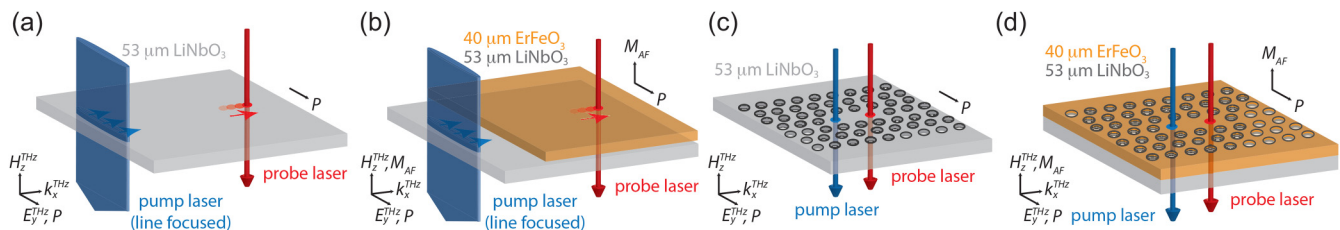

FIG. 1. Sample structures. (a) Bare LN waveguide. (b) Hybrid LN-EFO waveguide. (c) Bare LN PhC cavity. (d) Hybrid LN-EFO PhC cavity. For the cavity structures [(c) and (d)], pump and probe are focused in the "defect" region of the L3 cavity to generate and detect (magnon-)phonon-polaritons. For the unpatterned cases [(a) and (b)], we use a cylindrically focused pump, while the spatial probe position is varied along the *x*-direction. Note that the ferroelectric polarization *P* of LN is oriented always parallel to the *y* direction. In case of the hybrid sample structures [(b) and (d)], the net magnetic moment M_{AF} is oriented parallel to the *z*-axis.

additional $40\,\mu m$ thick (001) EFO slab, grown as a single crystal by the floating-zone method and cut to a size of $5 \times 5\,mm^2$, was used.[45–47] Both LN and EFO crystals were polished using diamond paste ($1\,\mu m$ grain size) to reach a surface roughness of less than 100 nm, which is less than 1/10 of the THz wavelength. Large sample planes were prepared with a parallelism accuracy below $1\,\mu m$. In case of the hybrid structures, a thin layer of air, approximately $8\,\mu m$ thick, separated the two slabs.

The bare LN slab acts as a waveguide and provides THz field confinement along the z-axis (out-of-plane axis), but for the cavity structures [see Figs. 1(a) and 1(c)], we also desire confinement in the x- and y-directions. To accomplish this, we utilized a photonic crystal cavity[48–50] (PhC) composed of a periodic array of air holes cut into the LN slab using femtosecond laser machining.[51] The cavity we fabricated, often referred to as an L3 cavity,[52] is composed of a hexagonal lattice of air holes with three holes absent from the array to form the "defect" cavity. To fabricate the hybrid LN-EFO cavity, we first attached the LN and EFO slabs together and then laser machined the cavity into the hybrid slab.

In LN, the material excitation is the polar lattice vibration (i.e., transverse optical phonon mode) with its polarization P along the (ferroelectric) c crystallographic axis of the tetragonal crystal (the y-axis as defined in Fig. 1). The electric-field component of a THz-frequency electromagnetic wave, oriented along the y-direction, coherently couples to these phonons to produce mixed phonon-polaritons.[42,53] Although the polaritons in our experiments are well detuned from the phonon resonance (the lowest transversal optical phonon resonance is located at $4.6\,THz$[88]), the phononic nature is still integral to the dynamics. Not only does the lattice carry $\sim 32\%$ of the energy in the 0.1–2 THz range (Appendix C), the phonon mode is also responsible mechanistically for efficient generation and detection of the THz waves in our experiments. In EFO, the relevant material excitation is the collective magnetic spin wave, i.e., the Brillouin zone center quasiantiferromagnetic (AF) magnon mode wherein the net magnetization M_{AF} along the c axis of the orthorhombic crystal (the z-axis as defined in Fig. 1) is modulated in amplitude.[41,54] The magnetic-field component of THz light along the z-axis coherently couples to the AF mode at the magnetic resonance transition frequency of $0.67\,THz$ (with no applied magnetic field) to produce mixed magnon-polaritons. In the hybrid samples, uniform y-electric-polarized, z-magnetic-polarized THz-frequency electromagnetic waves extend throughout both materials, resulting in new hybridized magnon-phonon-polariton modes.

B. THz polaritonics platform

To study the interaction, we performed pump–probe measurements using a Ti:Sapphire amplifier system (Coherent Inc.) that outputs 90 fs duration pulses with an 800 nm center wavelength at a 1 kHz repetition rate. The laser power was first split in a ratio of 90/10 for the pump and probe pulses, respectively. The pump pulse was variably delayed by time t, frequency doubled to 400 nm in a β-barium borate (BBO) crystal, and as shown in Figs. 1(a) and 1(b) focused into the bare LiNbO$_3$ portion of the slab to excite a y-electric-polarized, x-propagating phonon-polariton wavepacket via impulsive stimulated Raman scattering.[55] This process is also extensively exploited for high-field THz wave generation in LN.[56]

Our phonon-polariton wavepackets have about 0.1–2 THz spectral content. In the LN slab whose thickness (tens of μm) is on the order of the generated THz wavelengths (few tens to few hundreds of μm), the THz waves propagate in the plane of the slab as dielectric waveguide modes.[57] Due to the index mismatch between the phonon-polaritons and the optical pulse generating them, the phonon-polaritons also propagate laterally away from the generation region. To detect their progress, we exploit the electro-optic effect wherein the THz electric field modulates the LN refractive index.[58] More specifically, the lattice displacements of the optical phonon mode change the optical refractive index via electron–lattice interactions.[59] By passing a time-delayed optical probe pulse (typically at a different wavelength from the 400 nm pump) through the slab and measuring the THz-induced depolarization, the time-dependent THz electric-field profile can be obtained [see Fig. 2(a)]. The field profile can then be Fourier transformed to retrieve the frequency spectrum. If the probe pulse is spatially expanded and detected on a camera as shown in Fig. 2(b), we can also obtain a spatially resolved image of the THz wave. We thus have a platform for generating and detecting THz waves directly inside the LN slab.

III. RESULTS

A. Magnon-phonon-polaritons

To first study the interaction between magnons and phonons in the bare slabs, we performed pump–probe measurements on the unpatterned samples shown in Figs. 1(a) and 1(b). The 400 nm pump is cylindrically focused into the LN portion of the samples to excite y-electric-polarized, x-propagating phonon-polariton wavepackets, propagating away from the generation region. In the hybrid case, these waves enter into the hybrid LN–EFO slab. Here, the electric and magnetic fields of the THz wave, polarized along the y- and z-directions, respectively, drive the polarization of the polar phonon mode in LN and the magnetization of the AF magnon mode in EFO. In Fig. 3(a), we show a finite element method (FEM) simulation of electromagnetic wave transmission from the bare slab into the hybrid slab at 0.67 THz in the absence of any resonances (detailed simulations can be found in Appendix A). The transmission can be seen to proceed fairly efficiently, and a uniform electromagnetic mode can be seen extending through the slab(s), evanescently decaying away beyond either face of the structure. These waves are recorded via 800 nm probe pulses that were shifted spatially (along the x-direction) and time-delayed with respect to the pump, enabling spatiotemporal field characterization. A display of the profiles $E_y^{THz}(t)$ measured in successive sample locations appears as a 2D space-time matrix $E_y^{THz}(x, t)$ as shown in Fig. 3(b). Although the pump launches counterpropagating waves, initially we only observe the rightward traveling wave because the pump pulse is to the left of the detection window. The first several oscillation cycles of this wave are due to the lowest-order waveguide mode, and the second oscillation cycles are due to the next waveguide mode. Sometime later, we also observe an additional rightward propagating wave starting at $\approx 40\,ps$ and a leftward propagating wave starting at $\approx 90\,ps$ that are due to partial reflections at the edges of the sample. Finally, a 2D Fourier transform was performed to obtain the wavevector-frequency dispersion curve $E_y^{THz}(k_x, \omega)$.
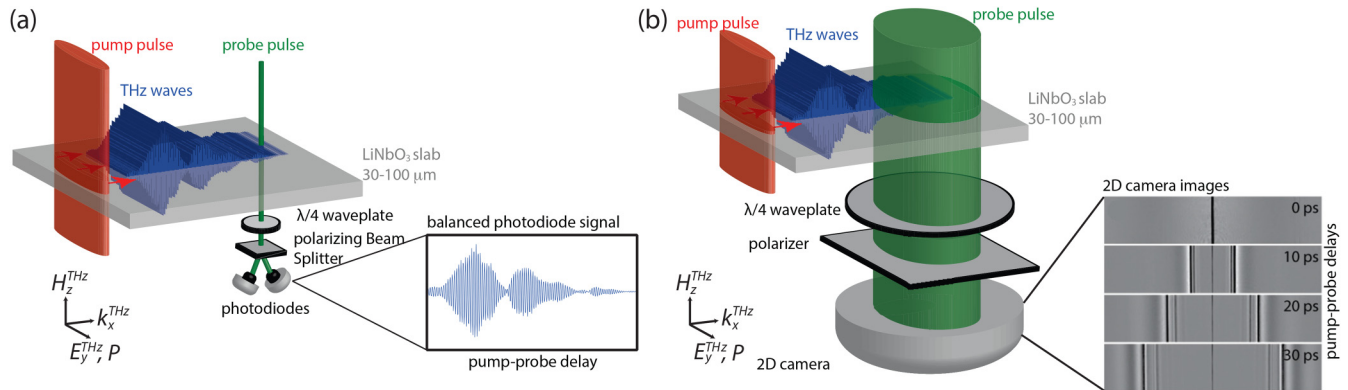
FIG. 2. THz polaritonics. (a) Localized point detection. A cylindrically focused optical pulse acts as a "line" source generating THz responses that propagate laterally within the LN waveguide. The THz waves may encounter, or be generated within, structures like the PhC fabricated into the LN. The THz evanescent field extends outside the LN slab. As shown in the inset, the balanced photodiode signal shows the time evolution of the THz electric field. (b) Image detection. As in the case of localized point detection, the THz waves are excited via a "line" source. The probe, however, is expanded to illuminate a large area of the LN slab and imaged onto a 2D charge coupled device (CCD) chip. As presented in the inset, this enables us to acquire real-space images of THz fields propagating in an unpatterned LN waveguide. Fourier transformation of the field amplitude vs the lateral position x and time delay t yields the waveguide mode dispersion curves.
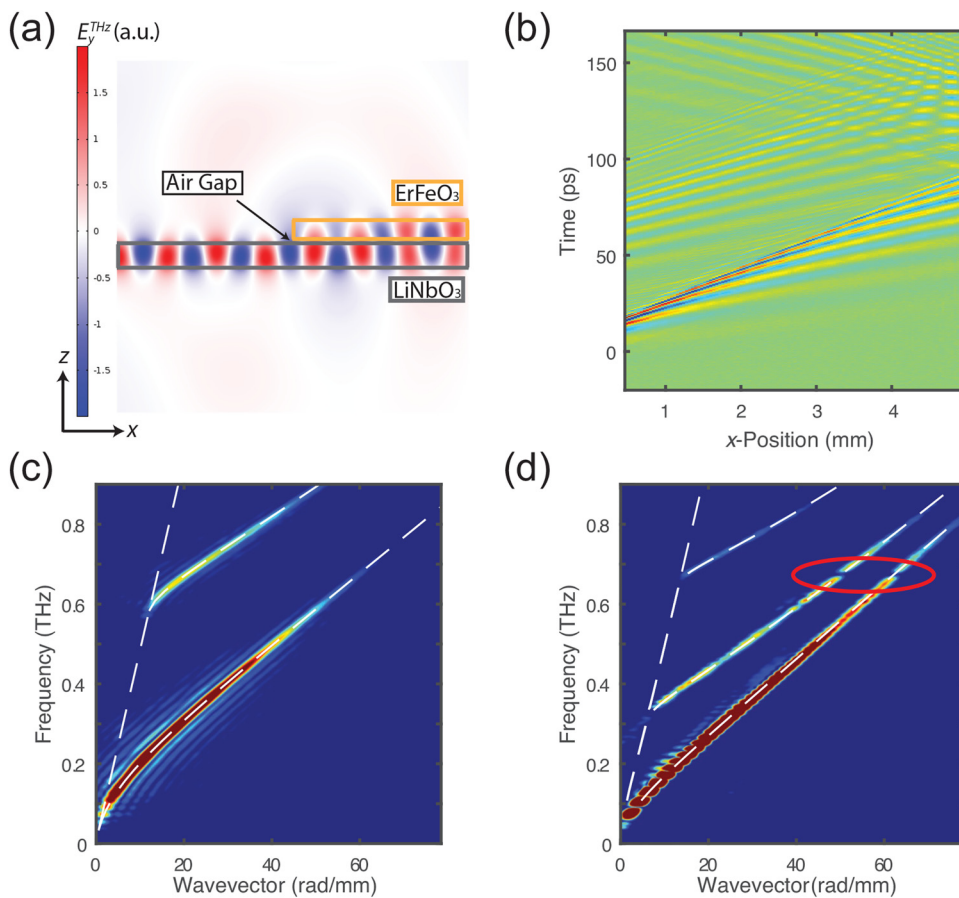

FIG. 3. Spatiotemporal detection of THz waveguide magnon-phonon-polaritons. (a) FEM simulation of electromagnetic wave transmission at 0.67 THz in the absence of the magnon resonance. The colormap of the out-of-plane electric-field profile is shown and corresponds to E_y^{THz}. (b) Space-time plot $E_y^{THz}(x, t)$ for the hybrid LN-EFO slab. At each position along the propagation direction, the time-dependent THz electric-field profile is displayed along the vertical axis. (c) Experimentally recorded TE-waveguide dispersion curves determined from measurements of the bare LN slab, showing the first two modes along with numerical solutions (dashed curves). (d) Experimentally recorded TE-waveguide dispersion curves for the hybrid LN-EFO structure, with a clear signature of an avoided crossing at the magnon resonance frequency of 0.67 THz in both the first- and second-order modes [highlighted with a red ellipse—for a detailed view, see Fig. 4(a)].

In Fig. 3(c), we show the experimentally recorded dispersion curve for the bare LN slab [Fig. 1(a)]. Owing to the almost linear dispersion of the THz phonon-polaritons in our THz pulse bandwidth, two well separated transverse-electric (TE) dielectric phonon-polariton modes appear,[57] showing almost linear dispersion within our THz pulse bandwidth. In Fig. 3(d), we show the experimentally recorded dispersion curves for the hybrid LN-EFO sample where three well separated modes appear. The existence of three modes in Fig. 3(d) compared to the two modes in Fig. 3(c) is a result of the increased thickness of the hybrid slab. For the proceeding analysis, we make two simplifications. Firstly, the existence of an air gap can be ignored as it does not significantly influence the dispersion curves (see Appendix A). Secondly, as demonstrated by the simulations, at most frequencies, the hybrid waveguide dispersion curves resemble those in a $93\,\mu$m slab of LN. This is because of the very similar refractive indices of LN ($n = 5.0$) and EFO ($n = 4.9$) for THz fields with the selected polarization. With these assumptions, we can focus on the notable feature in Fig. 3(d) near the magnon resonance at 0.67 THz: an avoided crossing in both the first and second-order waveguide modes.

The avoided crossing is a hallmark signature of strong coupling and can be explained by the formation of hybrid modes, the magnon-phonon-polaritons. In the following, we discuss this phenomena comprehensively by comparing a classical coupled oscillators' model with a Lorentz model.

1. Coupled oscillators' model

A phenomenological approach of coupled oscillators can be used to describe the interaction, using the Hamiltonian given as

$$H = H_{\mathrm{pp}} + H_{\mathrm{m}} + W_{\mathrm{int}}, \tag{1}$$

$$H = \hbar \begin{pmatrix} \beta c - i\kappa & 0 \\ 0 & 0 \end{pmatrix} + \hbar \begin{pmatrix} 0 & 0 \\ 0 & \omega_o - i\gamma \end{pmatrix} + \hbar \begin{pmatrix} 0 & \Omega/2 \\ \Omega/2 & 0 \end{pmatrix}, \tag{2}$$

$$\omega_{\mathrm{UP/LP}} = \frac{\beta c + \omega_o}{2} - i\frac{\gamma + \kappa}{2} \pm \sqrt{\Omega^2 + ((\beta c - \omega_o) + i(\gamma - \kappa))^2}. \tag{3}$$

Here, H_{pp} and H_{m} are the bare Hamiltonians and $\kappa = 12\,$GHz and $\gamma = 8\,$GHz[60] are the FWHM linewidths of the uncoupled phonon-polariton and magnon modes, respectively. W_{int} denotes their interaction, c is the speed of light in vacuum, ω is the eigenfrequency of the coupled system, $\omega_o/2\pi = 0.67\,$THz is the magnon resonance frequency, β is the hybrid waveguide wavevector that acts as the detuning parameter between the two bare modes via the term $\beta c - \omega_o$, and Ω is the splitting frequency, which is a measure of the coupling strength. Note that β can be defined in terms of the relation $\beta = n_{\mathrm{eff}}\omega/c$, where n_{eff} is termed the effective index and is defined as the ratio of the speed of light to the phase velocity of the waveguide mode. β thereby contains a frequency and a mode-dependent weighted average of the refractive indices of LN, EFO, and air. The solutions to this 2×2 Hamiltonian correspond to the upper and lower magnon-phonon-polariton branches ω_{UP} and ω_{LP}, respectively.

In Fig. 4(a), we show an enlargement of the LN-EFO hybrid slab dispersion curve for the first-order waveguide mode near the magnon resonance [see Fig. 3(d)], in which the avoided crossing feature can be seen clearly. The bare magnon and phonon-polariton modes are only well fitted to the experimental dispersion at large detunings, where the hybrid modes resemble the bare modes [Fig. 4(a), dashed lines]. In contrast, the upper and lower magnon-phonon-polariton branches from Eq. (3) are well fitted at all detunings, reproducing the normal mode splitting [Fig. 4(a), solid lines]. As a complement, in Fig. 4(b), we show the frequency spectrum for the first-order mode at a series of wavevectors spaced by 0.4 rad/mm and ranging from 61 to 65 rad/mm. The mode has phonon-polariton character at large detunings but shows a double-peaked structure at and near zero detuning where the magnon and phonon-polariton modes are strongly mixed. Although the second-order mode in Fig. 4(b) is far detuned for this range of wavevectors and thus shows a simple monotonic increase in center frequency, it also demonstrates a double-peaked spectrum at zero detuning. Similarly, Fig. 4(c) shows the frequency spectrum for the second-order mode at a series of wavevectors spaced by 0.4 rad/mm and ranging from 48.5 to 52.5 rad/mm. To confirm that the avoided crossing was due to the AF-mode magnon in EFO, we also performed temperature-dependent experiments (data not presented). We clearly observed the avoided crossing shift to 0.75 THz at 80 K, in agreement with the shift of the AF-mode magnon frequency in EFO.[60]

The splitting frequencies for the first and second-order waveguide modes were found to be $\Omega_1/2\pi = 20\,$GHz and $\Omega_2/2\pi = 18\,$GHz, respectively. Along with the linewidths for the magnon $\gamma/2\pi = 8\,$GHz and the phonon-polariton mode $\kappa/2\pi = 12\,$GHz, these allow us to estimate the cooperativity factor $C = \Omega^2/\kappa\gamma$. The cooperativity factor is a dimensionless quantity that compares the coupling strength to the losses in the system, with $C > 1$ considered strong coupling. The first and second-order phonon-polariton modes couple to the magnons with cooperativity factors $C = 4.0$ and $C = 3.4$, respectively, further validating that the system is in the strong-coupling regime.

2. Lorentz model

So far, we have used a classical coupled oscillator model for magnons and phonons because the two can be modelled as damped harmonic oscillators. A Lorentz model (i.e., linear dispersion theory) can also be used to describe the polariton formation. In this case, we assume that the permeability of EFO is modelled as a damped harmonic oscillator near the magnon resonant frequency. As such, the dispersion relation for the electromagnetic wave can be written as

$$\beta^2 c^2 = \omega^2 \mu_r \tag{4}$$

$$= \omega^2 \left(1 + \frac{\Delta\mu_r \omega_o^2}{\omega_o^2 - \omega^2 - i\gamma\omega} \right), \tag{5}$$

where we assume that $\Delta\mu_k = 8 \times 10^{-4}$.[60] Using this approach, we obtained a dispersion curve as overlaid on the data in Fig. 4(a) (green dash-dotted lines). Outside the anomalous frequency range,
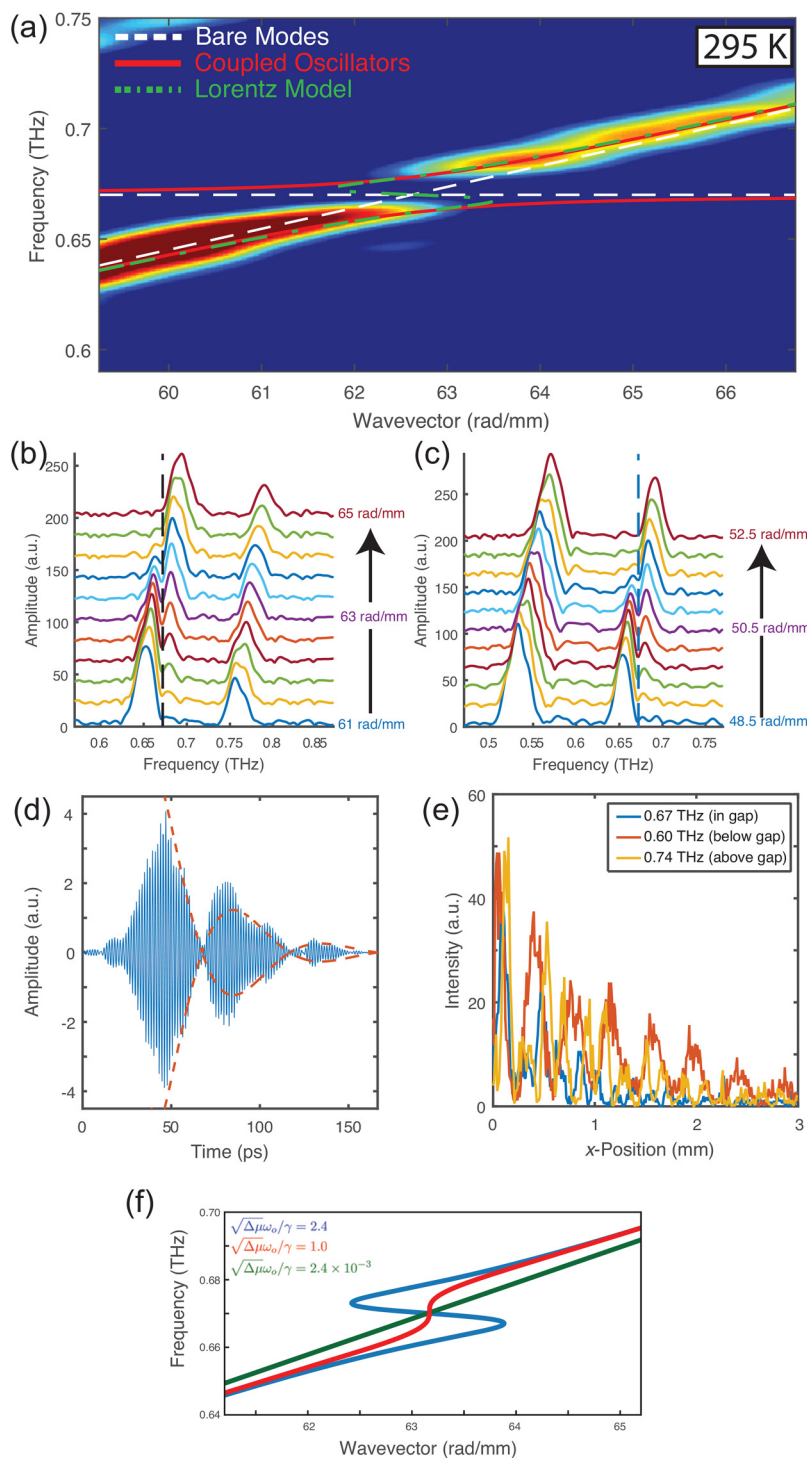
FIG. 4. Normal-mode splitting of THz magnon-phonon-polaritons. (a) Dispersion curve showing the normal-mode splitting between the magnon resonance at 0.67 THz and the first-order phonon-polariton mode. The white dashed curves show the uncoupled magnon frequency and a numerical calculation of the phonon-polariton dispersion, while the red solid and green dash-dotted curves show calculated magnon-phonon-polariton dispersion curves assuming a coupled oscillator model and a Lorentz model for the permeability of EFO, respectively. (b) and (c) Frequency spectrum at a series of wavevectors for the (b) first- and (c) second-order waveguide modes. The double-peaked structure in the first and second modes near the black dashed line, which indicates the magnon resonance at 0.67 THz, can be observed in (b) and (c), respectively. (d) Time-domain data obtained by frequency filtering of the 63 rad/mm spectrum shown in (b) to exclude all frequencies outside of the 0.60–0.73 THz range. (e) Spatial decay of the modes within, above, and below the bandgap of the avoided crossing. (f) Transition from weak to strong coupling as the ratio of oscillator strength to damping is increased. As the damping is reduced, linear dispersion transforms into a form approaching an avoided crossing.

the Lorentz model shows excellent agreement to the data and the coupled oscillator model of Eqs. (1)–(3). This is not surprising given that the Lorentz and coupled oscillator models are similar phenomenological approaches to describing strong light-matter coupling. The similarity comes from the fact that the electromagnetic field can be quantized as a harmonic oscillator or defined using dispersion relations. The discrepancy (anomalous dispersion vs an avoided crossing) comes from the fact that the Lorentz model

allows for a complex wavevector, i.e., spatial damping. This damping is the reason that the anomalous region was not seen in our experiments. In fact, in the absence of damping (i.e., $\gamma \sim 0$) and close to resonance (i.e., $\omega \sim \omega_o$), the Lorentz model is equivalent to the coupled oscillator model and its result can be written as

$$\omega_{\pm} = \frac{\beta c + \omega_o}{2} + \sqrt{\Delta\mu\omega_o^2 + (\beta c - \omega_o)^2}. \tag{6}$$

This has the same form as Eq. (3) in the absence of damping and also models an avoided crossing. In this case, the splitting frequency is given by $\sqrt{\Delta\mu_r\omega_o}/2\pi \simeq 19\,\text{GHz}$, which closely matches the experimentally extracted values for $\Omega_1/2\pi$ and $\Omega_2/2\pi$.

Despite the convergence of these two models, we should point out that light-matter interactions that allow for light propagation always have an associated complex wavevector, and strong light-matter coupling in these systems always exhibit anomalous dispersion. The Lorentz model is, therefore, often used to describe polaritons in bulk and waveguide geometries, while the coupled oscillator model is more suitable when the coupling occurs in a photonic cavity, for example. Interestingly, while both models are classical, they can also be used to describe the quantum observation of vacuum Rabi splitting.[14,61] The ability of these classical models to describe a quantum interaction stems from the fact that for weak atomic excitations, the quantum theory of interaction between an electromagnetic field and an atom is equivalent to the Lorentz model for a classical oscillator. Thus, to earn the distinction of quantum strong coupling, it is not sufficient to observe a splitting. Instead, a dependence of splitting energy on the electric field or the number of oscillators must be observed.[4,62] Such a dependence was not observed in our experiments but was observed in recent measurements on other samples.[63]

3. Energy exchange and bandgap

The strong coupling suggests that there is coherent energy exchange between the magnons and phonon-polaritons at a rate Ω. Our spatially and temporally resolved measurements permit direct observation of this process. Figure 4(d) shows time-dependent data at a selected wavevector of $\beta = 63\,\text{rad/mm}$, obtained by frequency filtering of the 63 rad/mm spectrum shown in Fig. 4(b) to exclude all frequencies outside of the 0.60–0.73 THz range, then inverse Fourier transforming to return to the time domain. This allows us to examine the evolution of only the lower-order waveguide mode at frequencies around the avoided crossing in order to illustrate the energy exchange clearly. Note that if there were no strong coupling, then there would be no hybridization and ensuing energy splitting between upper and lower polariton branches as outlined by Eqs. (3) and (6). In this case, there would only ever be a single mode at each wavevector; even on resonance, the magnon and phonon-polariton modes would be degenerate and hence not show any beating. Yet, in Fig. 4(d), we inspect the modes near 63 rad/mm, i.e., on resonance, and the signal shows beating with energy exchange period $2\pi/\Omega = 50\,\text{ps}$ and decay time $\tau = 2/(\kappa + \gamma) = 100\,\text{ps}$. This is a strong indication of the energy exchange between the two phonon-polariton and magnon components of the mixed magnon-phonon-polariton mode.[64]

Although the polariton bandgap in the hybrid waveguide excludes any eigenmodes around the bare magnon frequency, the phonon-polariton wavepacket entering from the LN extension includes frequencies within this forbidden gap. These waves decay exponentially into the hybrid slab. This can be explicitly seen by noting that the imaginary component of β in Eq. (5) can be explicitly written as

$$\text{Im}[\beta] = \frac{\Delta\mu_r\omega_o^2\gamma\omega}{(\omega_o^2 - \omega^2)^2 + \gamma^2\omega^2}. \tag{7}$$

The imaginary component of the wavevector corresponds to the inverse of the decay length into the slab. Ignoring other sources of absorption, the decay rate should be the greatest at the center of the gap (i.e., the bare magnon frequency) and the rate should decrease as frequencies at the gap edges are approached.[50] As shown in Fig. 4(e), the frequency component of 0.67 THz in the center of the bandgap has a decay length of 0.48 mm, 2–3 times shorter than those either above or below the bandgap, which have decay lengths of 1.27 mm and 1.32 mm, respectively. The frequency-dependent damping rates outside the forbidden range closely follow those of bare LN.[65]

We would also like to note that there exist THz-frequency phonon modes in EFO itself, and it was demonstrated that driving the modes in the infrared ($\approx 20\,\text{THz}$) can create an effective magnetic field that subsequently drives the AF-mode magnon.[36] However, this is a nonresonant Raman-type effect using $\approx$ MV/cm 20-THz field strengths. In contrast, we drive THz phonon-polariton waves in LN directly (primarily driving the ions through impulsive stimulated Raman scattering), and we use their magnetic-field component to resonantly drive the magnons in EFO. The driving of the magnons is thus linear in the THz field. In addition, in our system, the magnon response can be resolved through its coupling to the THz pulse at $\approx$ V/cm field strengths owing to the efficient electro-optic detection in LN.

4. Absorption, weak, and strong coupling

We use the term "strong coupling" in the manner broadly used in the literature to refer to strong light-matter coupling and the formation of polaritons, such as phonon-polaritons, plasmon-polaritons, exciton-polaritons, etc.[1,4] In this context, there is a clear distinction between simple linear absorption, i.e., weak coupling, and the strong-coupling regime, and the transition from one to the other is determined by the relative strength of the coupling compared to the losses in the system. In simple linear absorption, the coupling between the light and matter does not modify the dispersion except to reduce the light intensity at the absorption resonance, which in this case would be at the uncoupled magnon frequency. In the weak-coupling regime, the matter does indeed modify the dispersion but not in a way that produces two distinct coupled modes. In contrast, in the strong-coupling regime, the light and matter strongly interact and become hybridized modes at completely new frequencies, different from any uncoupled resonance frequency. We can use Eqs. (4) and (5) to demonstrate the difference between these regimes. In particular, in Fig. 4(f), we have plotted the dispersion relation of Eq. (5) for different ratios of magnon damping γ to oscillator strength $\Delta\mu_r\omega_o^2$, (the value in

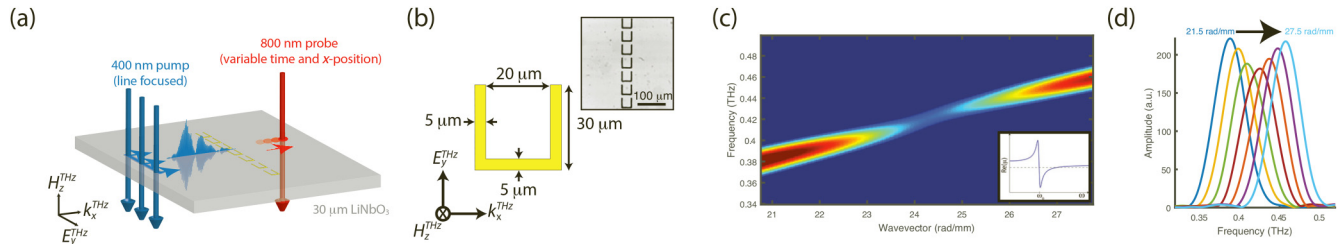**FIG. 5.** Linear absorption by an array of gold split-ring resonators with a magnetic resonance frequency of 0.42 THz fabricated on a slab of $30\,\mu m$ LN. (a) Geometry of the experiment demonstrating the acquisition of the spatiotemporal data after transmission through the array of SRRs. Associated polarizations of the THz electromagnetic field are also shown, where the y-axis corresponds to the c-axis of the LN crystal. (b) Dimensions of the SRR and the associated THz E- and H-field polarizations in the experiment. Inset shows a microscope image of the SRR array with a periodicity of $40\,\mu m$. (c) Dispersion curve near the magnetic resonance frequency, showing a minima in the absorption on resonance and no evidence of an avoided crossing. Inset shows SRR modeled by a Lorentzian model for the permeability. (d) Frequency spectrum at a series of wavevectors spaced by $1\,rad/mm$ and ranging from 21.5 to $27.5\,rad/mm$.

experiments was $\sqrt{\Delta\mu_r}\omega_o \simeq 2.4$). As the ratio is increased, linear dispersion is transformed into one approaching an avoided crossing. In reality, a true avoided crossing is only seen in the limit that the damping is small compared to the coupling/oscillator strength, such that Eq. (5) produces two solutions corresponding to the upper and lower hybridized polariton modes as specified by Eq. (6). Thus, strong coupling can be thought to occur when there are two solutions to Eq. (5) at a single wavevector with linewidths narrow enough to appear as distinct peaks, i.e., the birth of two hybrid modes. This transition occurs exactly at $\sqrt{\Delta\mu_r}\omega_o/\gamma = 1$, as evidenced in Fig. 4(f). Any ratio below this value can practically be considered to describe the weak-coupling regime, since there is still a deviation from a linear dispersion, yet there is still only a single peak evident for each wavevector.

To further demonstrate the point that the features in Figs. 4(a)–4(c) are not simply "gaps" in the dispersion curve due to linear absorption, we have performed an experiment that demonstrates the case of linear absorption due to a magnetic resonance by measuring the dispersion curve after transmission through an array of split-ring resonators (SRRs) patterned onto the surface of a $30\,\mu m$ LN slab (confer Fig. 5). The SRRs are 200 nm thick gold on a thin chromium adhesion layer deposited by optical lithography directly on the surface of the LN slab. Due to the orientation of the E- and H- fields in the experiment, the SRRs only exhibit a magnetic resonance that can be modelled using a Lorentz model for the magnetic permeability.[66] Thus, they permit close comparison to the AF-mode magnon in EFO. From the experimental dispersion curve of Fig. 5(c), there is no evidence of an avoided crossing. Instead, we observe a reduced amplitude around the resonant frequency. Furthermore, from the experimental wavevector-dependent spectra in Fig. 5(d), there is never a double-peaked structure. Instead, there is always a single peak whose magnitude is reduced when on resonance. This is the behavior expected for linear absorption and is demonstrably different from the avoided crossing shown in Fig. 4(a).

B. Cavity magnon-phonon-polaritons

The bare LN waveguide [Fig. 1(a)] provides THz field confinement along the z-axis (out-of-plane axis), but to build a cavity, we

also desire confinement in the x- and y-directions. To accomplish this, we utilized a photonic crystal cavity[48–50] composed of a periodic array of air holes cut into the LN slab using femtosecond laser machining.[51] The cavity we fabricated, often referred to as an L3 cavity,[52] is shown in Fig. 1(c) and is composed of a hexagonal lattice of air holes with three holes removed from the array to form the "defect" cavity. To excite the cavity modes, we focused pump pulses into the defect region of the crystal, which launched two counterpropagating THz phonon-polariton wavepackets. To detect the cavity polaritons, we directed probe pulses into the defect region and recorded the time evolution of the THz E-field as shown in Fig. 6(a) (imaging) and Fig. 6(b) (localized point detection). The wavepackets initially contain a broad range of frequencies as evidenced by a windowed FT [see Fig. 6(b), right]. When they reach the edges of the cavity, those waves with frequencies in the PhC bandgap are strongly reflected, while the rest of the frequency components are partially reflected due to the index mismatch with the surrounding PhC (i.e., Fresnel reflection). The bandwidth in the cavity thus narrows with every successive interaction with the holes, quickly approaching the limit where only the cavity modes are confined to the slab [see Fig. 6(b), right]. We also performed simulations for the E-field profiles within the cavity, which reveal that the different cavity modes have distinct spatial distributions. Since we use small focal spot sizes for the pump ($w_x \approx 10\,\mu m$, $w_y \approx 50\,\mu m$) and probe ($w_x \approx w_y \approx 10\,\mu m$) for the localized point detection measurements, their locations in the cavity determine the modes with which they predominantly interact. By choosing pump and probe to overlap with the extrema of a particular mode spatially, we can favor its generation and detection, respectively (see Appendix B).

Thus far, we have discussed the central role that the phonon mode plays in THz wave generation and detection, but the phononic nature of the polaritons is most easily seen by its influence on the cavity modes as a function of temperature. Firstly, the transverse optical phonon in LN is a soft mode associated with the ferroelectric phase transition at $T_c = 1418\,K$[68] at which the dielectric constant reaches a maximum. As a result, there is a sizable decrease in the THz refractive index from its room temperature values ($n_{eo} \approx 5$ and $n_o \approx 6.7$) to those at cryogenic temperatures.[69] As shown in Fig. 6(c), the decrease in the refractive index increases the
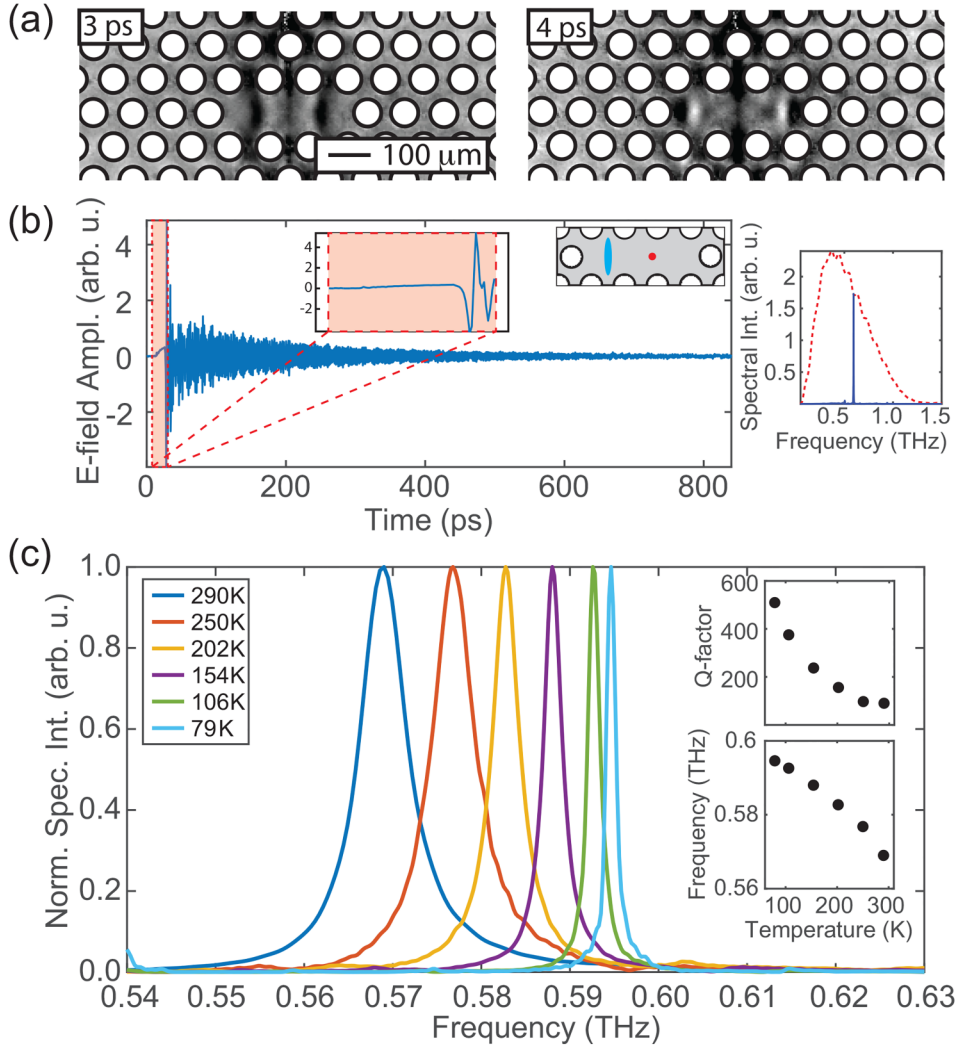
FIG. 6. THz-frequency phonon-polaritons in a bare LN PhC cavity. (a) Recorded electro-optic sampling images[67] of the bare LN PhC cavity at 3 and 4 ps after excitation, showing THz phonon-polaritons counterpropagating away from a pump pulse that irradiated the center of the PhC cavity (hexagonal array of air holes with radius $r = 29\,\mu m$ and periodicity $a = 100\,\mu m$, three removed air holes in the center for the "defect"). (b) The left figure is a time trace of the THz E-field in the cavity, recorded by fixing the locations of the pump and probe beams as shown by the blue line and the red spot, respectively, in the inset. The red dashed lines indicate an approximate time window during which the initial THz wavepacket is passed by the probe pulse (note the zoomed region inset). The right figure shows the spectral intensity of the windowed region (red dashed line) and the entire time trace (blue solid line), demonstrating that the initial broad bandwidth is narrowed to that of the cavity mode. (c) The temperature-dependent spectra for the X2 cavity mode (see Appendix B) demonstrate the influence of the soft transverse optical phonon mode in LN. As the temperature is reduced, the refractive index and phonon damping decrease and this causes, respectively, an increase of the mode frequency and a decrease of the mode linewidth. Inset shows the temperature dependence of the Q-factor and resonant frequency.

cavity mode frequency ($\Delta\omega/\omega \sim \Delta n/n$[50]). Secondly, the damping of the low-frequency phonon-polaritons in LN is mainly attributed to a coupling of the TO phonon to other low-frequency phonon modes.[70,71] This damping is reduced by a factor of ≈ 5 from 290 K to 79 K as the low-frequency phonon modes become depopulated.[69,72] The effect on the cavity modes can be deduced from Fig. 6(c), where the mode linewidth is also reduced by a factor of ≈ 5. To analyze this change more quantitatively, we use a common measure of the cavity lifetime called the quality factor $Q = \omega_{cav}/\kappa$, where ω_{cav} is the resonant frequency of the mode and $1/\kappa$ is the rate of energy loss from the cavity.[73] The quality factor can be interpreted as a dimensionless lifetime that can account for the combined contributions from the intrinsic damping Q_m and radiative scattering of light out of the cavity Q_r leading to a net Q_{net} defined as $1/Q_{net} = 1/Q_m + 1/Q_r$. In our case, the increase in Q_{net} with decreasing temperature is directly proportional to the decrease in phonon damping since this is the dominant mechanism limiting

the lifetime, i.e., $Q_m \ll Q_r$, so $Q_{net} \simeq Q_m$. Hence, in our experiments, the highest $Q = 510$ was obtained at our lowest recorded temperature of 79 K. Based on the temperature dependence of the phonon absorption coefficient of LN, the Q can be increased further to $Q \simeq 1000$ at 4K.[72] Another important measure of the cavity is the effective mode volume V_{eff}, defined as

$$V_{eff} = \frac{\int \epsilon(\boldsymbol{r})|\boldsymbol{E}(\boldsymbol{r})|^2 d^3\boldsymbol{r}}{\max\left[\epsilon(\boldsymbol{r})|\boldsymbol{E}(\boldsymbol{r})|^2\right]}. \quad (8)$$

For the so-called X1 mode (Appendix B), $V_{eff} = 3.4 \times 10^{-3}\lambda^3 \simeq 0.5(\lambda/n)^3$, where λ is the free-space wavelength and $n = 5.21$ is the average refractive index of the slab. Although the effective mode volume is not appreciably smaller than the $(\lambda/n)^3$, the large refractive index of the LN slab at THz frequencies results in a mode volume that is nearly three orders of magnitude smaller than the free-space volume.

Having established the particulars of our LN based cavity, we now discuss our experiments regarding the collective strong coupling between magnons, phonons, and cavity photons in a hybrid L3 PhC cavity, depicted in Fig. 1(d). Our system consists again of a thin composite slab of $53 \mu m$ thick (100) LN and $40 \mu m$ thick (001) EFO. As before, the PhC cavity was fabricated using laser machining to cut hexagonal array of air holes through the hybrid slab. The E-field component of the THz light, polarized along the z-direction, can couple to the phonons in LN to produce mixed phonon-polariton modes. Simultaneously, the H-field component of light, polarized along the z-axis, can couple to the AF mode of EFO to produce mixed magnon-polaritons. In the hybrid cavity, a contiguous y-electric-polarized, z-magnetic-polarized THz-frequency electromagnetic wave can extend throughout both materials, forming new hybridized cavity magnon-phonon-polariton modes (see Appendix B for hybrid slab FEM simulations).

To verify the formation of cavity magnon-phonon-polariton modes, we studied the frequency spectrum of the THz waves as the frequencies of the cavity and magnon modes were tuned by varying the temperature. While we have seen that the cavity resonance of the pure LN shifts upon reduction of the temperature from 290 K to 77 K by ≈ 18 GHz in a weakly quadratic fashion [see the inset of Fig. 6(c)], the magnon resonance shifts by ≈ 80 GHz and does so with a higher-order functional form.[60,74] To record the frequency spectrum, we generated and detected THz waves in the LN portion of the hybrid cavity [see Fig. 7(a)]. Despite being excited in LN, the THz waves evolve into the modes that span the entire hybrid structure. Thus, there exists an E-field parallel to the polar lattice vibration in LN and an H-field parallel to the antiferromagnetic magnetization in EFO. However, electro-optic probing is only sensitive to the E-field in LN and can, therefore, only detect the AF-mode magnon response through its interaction with the cavity mode. As shown in Fig. 7(b), at 290 K we only observed a single
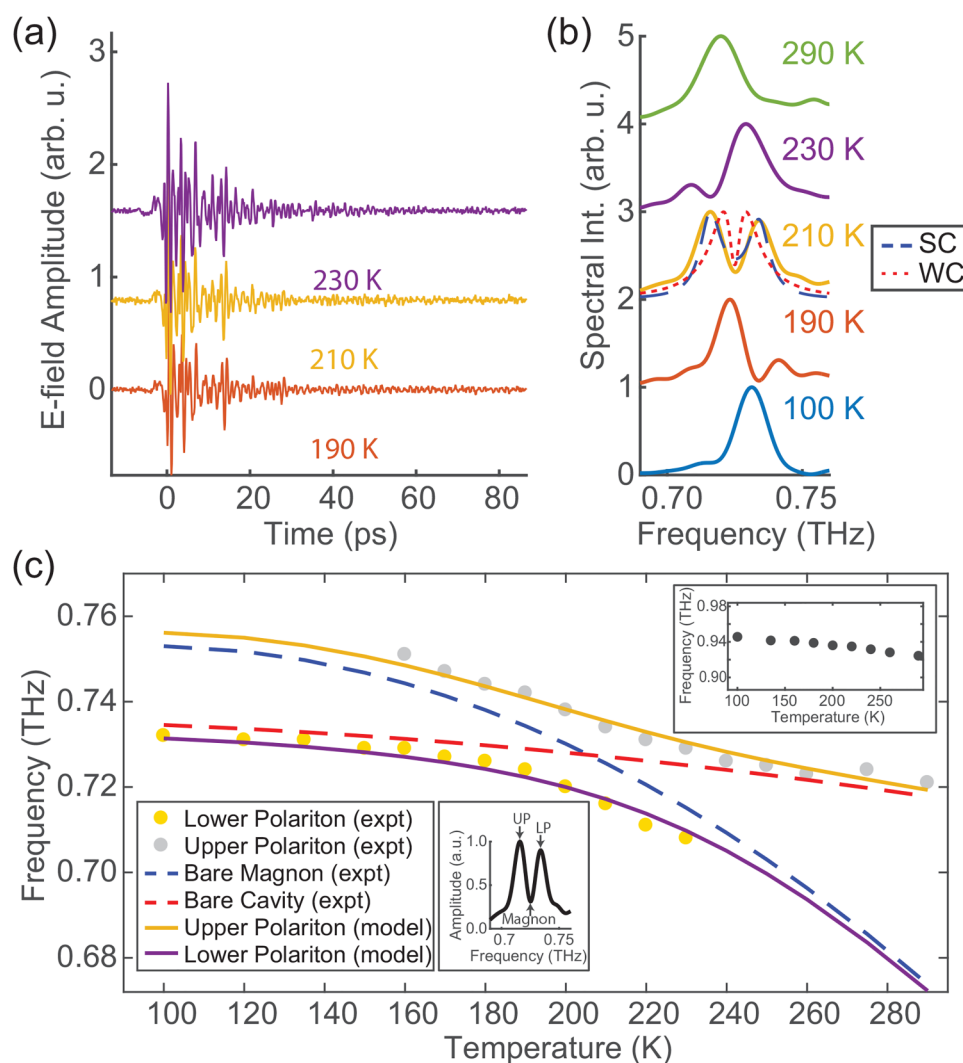

FIG. 7. THz-frequency magnon-phonon-polaritons in the hybrid LN-EFO PhC cavity. (a) Temperature-dependent time traces of the THz E-field in the hybrid cavity. Traces are vertically offset for clarity. (b) THz spectra near the X1 cavity mode. The double-peaked spectrum in the range of $170 - 230$ K demonstrates the presence of a normal-mode splitting between upper and lower polariton modes. The dashed and dotted lines overlaid at 210 K correspond to models for strongly coupled oscillators (SC) and THz absorption by the magnon mode in the weak-coupling limit (WC), respectively. (c) Avoided crossing of cavity magnon-phonon-polaritons. The upper and lower polariton mode frequencies are plotted as a function of temperature. The solid lines correspond to the collective strongly coupled oscillator model while the dashed lines correspond to the bare magnon and cavity frequencies. The bottom left inset shows the locations of the upper (UP) and lower (LP) polariton frequencies in the cavity spectrum at 210 K, and also indicates the bare magnon frequency. The top right inset shows the weakly quadratic temperature dependence of a higher-frequency cavity mode, which was used to determine the temperature dependence of the hybrid waveguide refractive index and from that the bare cavity mode that is resonant with the magnon mode (red dashed line).

Lorentzian peak corresponding to the cavity mode at 0.72 THz and did not observe the magnon mode at 0.67 THz, which was sufficiently detuned such that any interaction with the cavity mode was negligible. However, as the temperature was reduced and thus the two modes were tuned to be in resonance, a clear double-peaked spectrum appeared. At 210 K, the detuning between the bare modes was only 2 GHz, yet we observed two peaks that were separated by nearly eight times the detuning. This double-peaked structure is characteristic of a normal-mode splitting that can arise from the strong coupling between the cavity and magnon modes.

Like in the unpatterned case, the interaction can be modeled using the Hamiltonian for coupled oscillators given by

$$H = H_{cav} + H_o + W_{int}, \tag{9}$$

$$\omega_{UP/LP} = \frac{\omega_{cav} + \omega_o}{2} - j\frac{\gamma_{cav} + \kappa_{cav}}{2}$$
$$\pm \sqrt{\Omega_{cav}^2 + [(\omega_{cav} - \omega_o) + j(\gamma_{cav} - \kappa_{cav})]^2}. \tag{10}$$

Here, H_{cav} and H_o are the bare Hamiltonians for, respectively, the cavity and magnon modes, and W_{int} denotes their interaction. Correspondingly, $\omega_o/2\pi$ and γ_{cav} are the magnon resonance frequency and linewidth, and ω_{cav} and κ_{cav} are the cavity resonant frequency and linewidth, respectively. Finally, Ω_{cav} is the splitting frequency and the only undetermined parameter in the equations. The solutions to this Hamiltonian correspond to the upper and lower magnon-phonon-polaritons ω_{UP} and ω_{LP}, respectively. As shown in Fig. 7(b) by the blue dashed curve, the coupled oscillator model (SC) shows excellent agreement with our data and indicates that the phonon, magnon, and cavity photons are no longer the eigenmodes of the system. Instead, the THz response leads to collective mode oscillation at the frequency Ω_{cav} between a state wherein the energy is stored purely in the light field and phonons in LN and a state wherein the energy is stored purely in the magnons in EFO. Note that these spectra are distinctly different from the result of simple THz absorption by the magnon resonance in EFO. The magnon linewidth is far narrower than the splitting we observe between the upper and the lower polariton peaks, as shown in Fig. 7(b). Absorption at the magnon frequency would also yield a double-peaked structure around that frequency due to the magnon FID induced in the weak-coupling (WC) limit by the THz field generated in LN. However, in this case the separation between the two peaks would be given by the magnon absorption linewidth [simulation shown in the red dotted curve of Fig. 7(b)] rather than the strength of the coupling. The actual spectrum we measure and the model based on strong coupling (blue dashed curve) show a far larger separation between the two THz spectral peaks.

By identifying the lower and higher-frequency peaks as, respectively, the upper and lower polaritons, we generated a plot for the two branches as a function of the temperature, as shown in Fig. 7(c). The curves for the coupled oscillator modes and bare cavity and magnon modes are also overlaid in Fig. 7(c). The temperature dependence of the bare magnon frequency was recovered from the minima in the frequency spectra [Fig. 7(c), bottom left inset] and agrees well with previous results.[60,74] The temperature

dependence of the bare cavity frequencies was determined from a second cavity mode that showed the same dependence [Fig. 7(c), top right inset]. The bare frequency values were used to calculate the upper and lower polariton branches with Ω_{cav} as the fitting parameter. The coupled oscillator model agrees well with the data at all detunings and reveals the existence of an avoided crossing between the two branches, a hallmark signature of strong coupling. From the two branches, we determined the splitting frequency at zero detuning to be $\Omega_{cav}/2\pi = 16$ GHz. Utilizing the splitting frequency and the linewidths for the magnon $\gamma_{cav}/2\pi = 7$ GHz and cavity mode $\kappa_{cav}/2\pi = 14$ GHz at zero detuning, we also estimated the cooperativity factor $C_{cav} = 2.6$ for our data. This further supports the assertion that we reached the collective strong-coupling regime.

These results agree well with our above presented results for the hybrid slab without the PhC cavity ($\Omega/2\pi = 18$ GHz; $\gamma/2\pi = 8$ GHz; $\kappa/2\pi = 12$ GHz; $C = 4.0$). The slight differences arise due to the different temperatures and pump intensities, since we slightly reduced the pump intensity to avoid damage to the hybrid PhC structure. At first glance, this agreement might come as a surprise since one expects an increase in coupling strength due to the cavity. However, the collective normal-mode splitting Ω_{cav} of the magnon-phonon-polariton in the hybrid cavity is scaling with the square root of the ratio of the number of oscillators N and the mode volume V, i.e., $\Omega \propto \sqrt{N/V}$.[3,75] Indeed, by fabricating the cavity into the hybrid slab of EFO and LN, we decrease V, but since we are in the solid phase, we also decrease N by the same factor. Hence, we expect the same coupling strength as in the unpatterned hybrid slab. In addition, note that the quality factor of the hybrid cavity mode ranged from $Q = 42$ at room temperature to $Q = 56$ at 100 K. This was smaller than in our bare LN cavity and was attributed to both damping from the EFO and significant radiative scattering. The radiative scattering is not entirely surprising given the difficulty of laser machining high-quality air holes through a composite structure. Nonetheless, our Q was sufficient to reach the collective strong-coupling regime, i.e., $C > 1$.

IV. CONCLUSION

We have demonstrated evidence for collective strong coupling among magnons, phonons, and photons at THz frequencies using a unique on-chip platform. For the unpatterned LN-EFO hybrid slab, we have observed an avoided crossing in the dispersion curve for both the first- and the second-order TE dielectric waveguide modes, which exhibit a normal-mode splitting of $\Omega_1/2\pi = 20$ GHz and $\Omega_2/2\pi = 18$ GHz with corresponding cooperativity factors $C = 4.0$ and $C = 3.4$, respectively. Correspondingly, in the time domain, we observed a beating between the upper and the lower magnon-phonon-polaritons with an oscillation period of $2\pi/\Omega = 50$ ps, which is the period for energy exchange between phonons and magnons. In the spatial domain, we observed evanescent wave decay at frequencies within the bandgap as the wavepacket entered the hybrid waveguide. For the bare LN cavity, we found strongly coupled admixtures of phonons and cavity photons exhibiting a Q-factor of 510 at 79 K (the lowest temperature studied) and a mode volume of $V = 3.4 \times 10^{-3}\lambda^3 \simeq 0.5(\lambda/n)^3 \, \mu m^3$. The Q-factor

is limited by the phononic damping and could be increased to $Q \simeq 1000$ at 4 K. Furthermore, we could demonstrate collective strong coupling in a hybrid cavity composed of LN and EFO. Using temperature tuning of the cavity and magnon modes, we observed a normal-mode splitting of 16 GHz, an avoided crossing between the upper and the lower polariton branches, and a cooperativity factor of $C = 2.6$, confirming that we reached the collective strong-coupling regime. The data also show excellent agreement with a coupled oscillator model. These observations are understood as evidence for the formation of cavity magnon-phonon-polaritons, wherein phonons in the LN and magnons in the EFO are coupled to the EM wave E- and H-fields, respectively, as they are in the unpatterned hybrid waveguide.

Our demonstration illustrates a system with multifunctional capabilities that should prove promising for realizing ultrafast THz cavity spintronics. For instance, EFO enables long-term storage and all-optical addressing of spin states. As a complement, LN has large electro-optic constants that enable efficient generation and detection of THz waves,[76,77] with prospects for both spatial and temporal shaping of the THz field profile,[42,53] e.g., via chirp-and-delay of the generating femtosecond laser pulse,[78] and prospects for various forms of electrical control.[79] The coupling to THz light in a waveguide also allows coherent propagation of the magnetization in a highly confined and efficient manner. Our cavity is able to achieve a Q-factor comparable to that of another THz cavity recently used in strong-coupling work,[26] but in a much smaller mode volume that is nearly diffraction limited. The femtosecond laser machining process could be used to fabricate other cavity geometries with considerably smaller model volumes.[80] Another useful feature is that the Q-factor can be increased without degrading the THz signal injection and readout, since these are achieved via optical-frequency light directly inside the cavity. We believe our approach may prove valuable for experiments pursuing THz cavity QED. These experiments require high Q and low V because the vacuum Rabi frequency must be fast compared with the cavity loss rate and decoherence processes. A high Q minimizes decoherence, while a lower V increases the Rabi frequency ($\Omega \sim 1/\sqrt{V}$). There has already been some progress in using electro-optic crystals similar to LN to measure the quantum properties of light at THz frequencies.[81–83] Combining this methodology with our cavity should enable the demonstration of THz cavity QED phenomena in the future.

The on-chip cavity platform might prove useful also for other applications like sensing and spectroscopy, e.g., by depositing liquid or solid samples into unpatterned LN slabs or cavities. The dual-waveguide geometry used here is one example of how a sample could be coupled to a LN waveguide for linear or nonlinear THz spectroscopy with no free-space THz propagation, relying on LN for THz generation and detection. While the hybrid cavity demonstrated here confined the THz polariton field in all three dimensions, cavities with one or two unconfined dimensions can also be created by fabricating two photonic structures with a region between them whose width could be an $(n + 1/2)$ multiple of the desired cavity resonance wavelength, with the overall thickness of the structure dictating the extent of confinement in the z dimension through index contrast with the surrounding free space. The dispersion properties of such cavities

closely resemble those of the microcavities used in studies of exciton-polaritons.[84,85] It is straightforward to see that the effective mass of magnon-phonon-polaritons in such cavities can be as small as $10^{-7} m_e$, about two orders of magnitude lower than the typical value for exciton-polaritons. The corresponding de Broglie wavelength $\lambda_{th} = h/\sqrt{2\pi m k_B T}$ can be approximately $10 \mu m$ at room temperature and $> 50 \mu m$ at low but not ultralow temperatures, ≈ 10 K. This indicates that magnon-polariton Bose–Einstein condensation should be achievable at quite low excitation densities, with interesting prospects for fundamental study and possible applications in quantum simulation, low-power coherent THz sources, and other areas.

APPENDIX A: SIMULATED DISPERSION CURVES AND FIELD PROFILES FOR THE UNPATTERNED SAMPLES

In the main text, we show a finite element method (FEM) simulation of electromagnetic wave transmission from the bare LN slab into the hybrid LN-EFO slab at 0.67 THz in the absence of any resonances [Fig. 3(a)]. Correspondingly, in Figs. 8(a) and 8(b), we show the FEM calculated field profile for the first-order waveguide modes in bare and hybrid structures at 0.67 THz, respectively. In both the single and hybrid waveguides, a uniform electromagnetic mode can be seen extending through the slab(s) and evanescently decaying away on either side of the structure, illustrating that both samples are acting as THz waveguides. Furthermore, the existence of three modes for the hybrid slab in comparison with two modes for the pure LN slab is a result of the increased thickness as demonstrated in Fig. 8(c), which shows that the waveguide modes become lowered in frequency and more closely spaced as the thickness of the waveguide is increased. We also discuss in the main text two simplifications for the analysis of the dispersion curves. Firstly, the existence of an air gap can be ignored as it does not significantly influence the dispersion curves, as can be seen in Fig. 8(d). Secondly, as demonstrated by Fig. 8(e), at most frequencies, the hybrid waveguide dispersion curves resemble those in a $93 \mu m$ slab of LN, due to the very similar refractive indices of LN ($n = 5.0$) and EFO ($n = 4.9$).
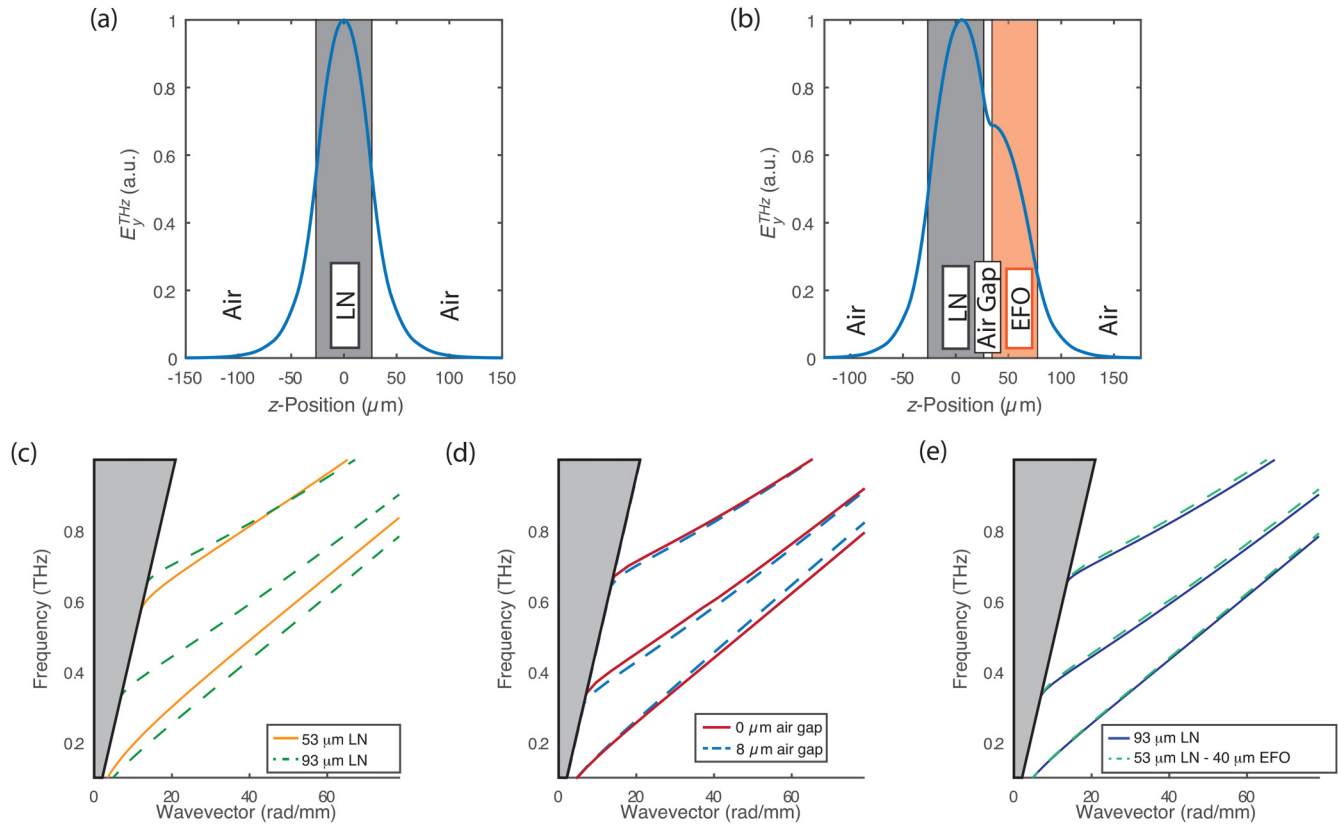
FIG. 8. FEM simulation of electromagnetic waveguide modes in the unpatterned samples. The data are simulated at 0.67 THz in the absence of the magnon resonance. (a) Calculated E_y^{THz} field profile for the first-order waveguide modes in the bare $53\,\mu m$ LN slab and (b) hybrid $53\,\mu m$ LN $- 8\,\mu m$ air $- 40\,\mu m$ EFO structure. (c) Calculated dispersion curves in the absence of the magnon resonance for a LiNbO$_3$ slab (with $n = 5.0$) of thickness $53\,\mu m$ or $93\,\mu m$. (d) Dispersion curves for a hybrid structure of $53\,\mu m$ LN $- 8\,\mu m$ air ($n = 1.0$) $- 49\,\mu m$ EFO ($n = 4.9$) and $53\,\mu m$ LN $- 49\,\mu m$ EFO (i.e., without air gap) demonstrate the minimal influence of an air gap. (e) Dispersion curves for a $93\,\mu m$ LN slab and a hybrid $53\,\mu m$ LN $- 49\,\mu m$ EFO structure are very similar.

APPENDIX B: SIMULATED ELECTROMAGNETIC-FIELD PROFILES OF THE CAVITY MODES

We also performed FEM simulations for the cavity structures. In Fig. 9(a), we show the simulated E-field profiles for the two cavity modes, labeled X1 and X2, in the bare LN PhC cavity. In general, the cavity modes have distinct spatial distributions, with the higher-frequency modes exhibiting a higher number of nodes and extrema.[86] Correspondingly, the simulated E_x-field and H_z-field profiles for the X1 cavity mode are shown in Fig. 9(b). The E-field component of the light, polarized along the z-direction, can couple to the phonons in LN to produce mixed phonon-polariton modes. Simultaneously, the H-field component of light, polarized along the z-axis, can couple to the AF mode of EFO to produce mixed magnon-polaritons.

Due to the small focal spot size of the pump ($w_y \approx 10\,\mu m$, $w_z \approx 50\,\mu m$) and probe pulses ($w_y \approx w_z \approx 10\,\mu m$) in our experiments, their locations in the cavity determine the modes with which they predominantly interact. By choosing pump and probe

pulses to overlap spatially with the extrema of a particular mode, we can favor its generation and detection, respectively. For instance, in Fig. 9(c), we show the frequency spectrum where we selectively excited and detected either the X1 or the X2 mode.

APPENDIX C: ENERGY DISTRIBUTION BETWEEN THE LATTICE AND THE ELECTROMAGNETIC WAVE

To calculate the energy distribution between the lattice motion and the electromagnetic field, we begin by describing the coupling between the transverse polar optic phonon mode and the electromagnetic field. The coupled equations are given as[87]

$$P = \omega_{TO}\sqrt{\epsilon_o(\varepsilon_o - \varepsilon_\infty)}Q + \epsilon_o(\varepsilon_\infty - 1)E, \quad (C1)$$

$$\ddot{Q} = -\omega_{TO}^2 Q - \Gamma\dot{Q} + \omega_{TO}\sqrt{\epsilon_o(\varepsilon_o - \varepsilon_\infty)}E. \quad (C2)$$

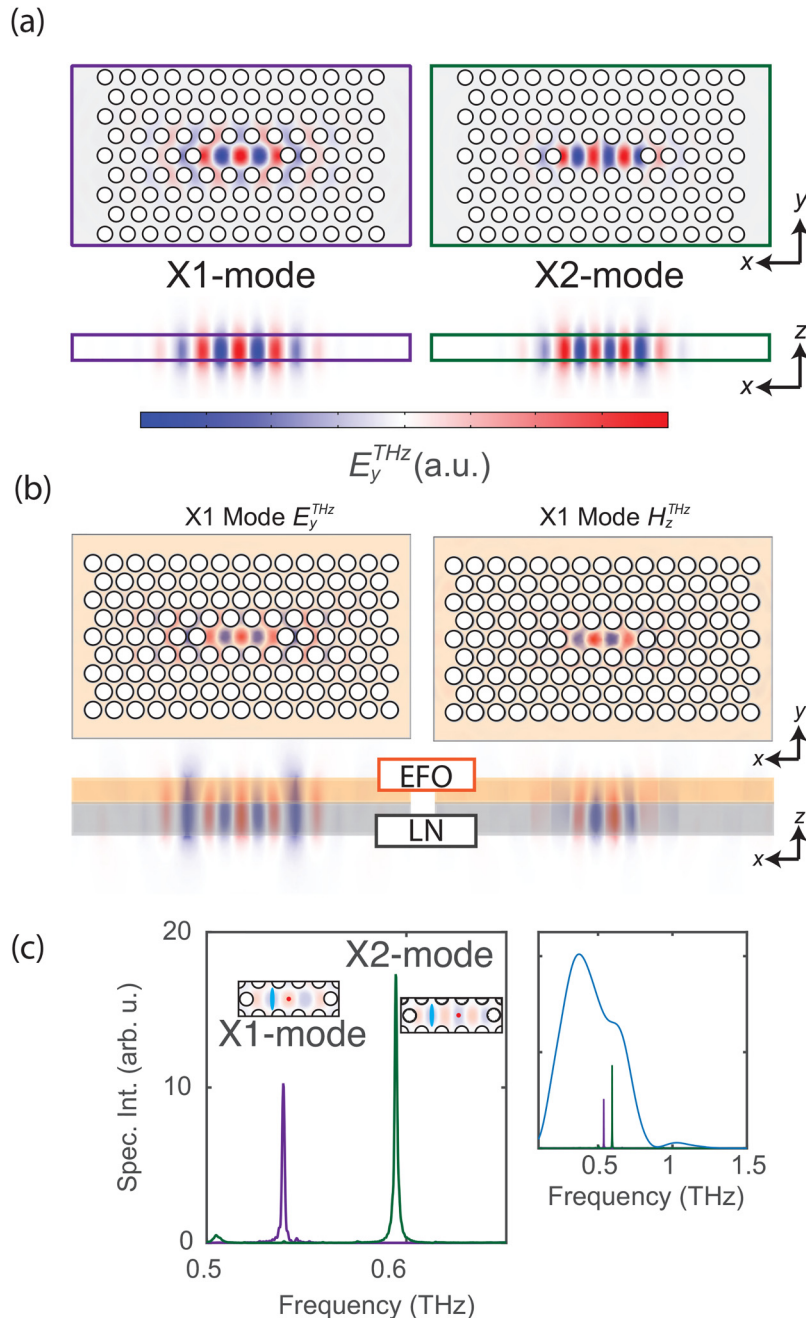Here, P is the macroscopic polarization of the material and Q is the

FIG. 9. Simulation of L3 PhC cavity modes. (a) FEM simulations of the mode profiles for two PhC cavity modes (air holes: radius $r = 29\,\mu$m, periodicity $a = 100\,\mu$m) denoted X1 and X2 in the bare LN PhC cavity. The color map corresponds to the z-polarized electric-field distribution. (b) FEM simulation of the X1 mode profile in the hybrid LN-EFO PhC cavity (air holes: radius $r = 29\,\mu$m, periodicity $a = 74\,\mu$m). The left image shows the y-polarized electric-field distribution, and the right shows the z-polarized magnetic-field distribution. (c) The left figure shows the frequency spectrum after selective interaction with either the X1 or the X2 mode in the bare LN PhC cavity, with accompanying insets that show the locations of pump (blue) and probe (red) beams. The right figure compares the narrow linewidths of the cavity modes to the broad spectrum in the bare LN waveguide [see Fig. 6(b) of the main text].

normalized ionic displacement of the polar optic phonon mode where an over-dot indicates the time derivative. In addition, ω_{TO} is the transverse optic phonon frequency, ϵ_o is the vacuum permittivity, and ε_∞ and ε_o are the high- and low-frequency dielectric constants of the material, respectively. Poynting's theorem relates the energy stored in the electromagnetic field to the work done on the electric dipoles in the medium. In differential form, the energy

balance can be expressed as

$$-\nabla \cdot S = \dot{W}, \qquad (C3)$$

where S is the Poynting vector and W is the energy density. Equation (C3) states that the rate of energy decrease in the medium is equal to the amount of energy flow out of the medium. To

determine the energy distribution between the lattice and the electromagnetic field, we must determine an appropriate energy density that satisfies Eq. (C3). Such an energy density was proposed by Huang[87] in the absence of damping ($\Gamma = 0$), which is given as

$$W = \frac{1}{2}\left(\dot{Q}^2 + \omega_{TO}^2 Q^2\right) + \frac{1}{2}\left(\epsilon_o \varepsilon_\infty E^2 + \mu_o H^2\right), \quad (C4)$$

where E and H are the electric and magnetic fields, respectively, Q is the normalized displacement of the phonon mode, and μ_o is the vacuum permeability. The first term in brackets of Eq. (C4) represents the vibrational energy of the TO phonon mode, given as a sum of the harmonic oscillator and potential and kinetic energy terms. The second term in brackets represents the electromagnetic energy, with an inclusion of the electronic response via the term ε_∞. As such, we can write the time-averaged energies in the lattice and electromagnetic wave as

$$\langle W_{latt}\rangle = \frac{\omega_{TO}^2 \epsilon_o (\varepsilon_o - \varepsilon_\infty)(\omega^2 + \omega_{TO}^2)}{4(\omega_{TO}^2 - \omega^2)^2}|E_o|^2, \quad (C5)$$

$$\langle W_{EM}\rangle = \frac{1}{4}\left(\epsilon_o \varepsilon_\infty + \frac{1}{\mu_o}\left(\frac{k}{\omega}\right)^2\right)|E_o|^2. \quad (C6)$$

The time-averaged fraction of mechanical energy in the mode is then given as

$$\langle \rho \rangle = \frac{\langle W_{latt}\rangle}{\langle W_{latt}\rangle + \langle W_{EM}\rangle}, \quad (C7)$$

where $\langle W_{latt}\rangle$ and $\langle W_{EM}\rangle$ are the time averaged lattice and electromagnetic energies, respectively. Using Eqs. (C5) and (C6) and assuming material parameters for LN as specified in the work of Feurer et al.,[53] the fraction of energy in the lattice is 32% at 1 THz.

REFERENCES

[1]L. C. Kwek, A. Auffèves, D. Gerace, M. Richard, S. Portolan, M. F. Santos, L. C. Kwek, and C. Miniatura, *Strong Light-Matter Coupling: From Atoms to Solid-State Systems* (World Scientific, Hackensack, NJ, 2014).

[2]D. L. Mills and E. Burstein, "Polaritons: The electromagnetic modes of media," Rep. Prog. Phys. **37**, 817–926 (2001).

[3]D. Snoke, "The connection of polaritons and vacuum Rabi splitting," preprint arXiv:1509.01468 (2015).

[4]P. Törmä and W. L. Barnes, "Strong coupling between surface plasmon polaritons and emitters: A review," Rep. Prog. Phys. **78**, 013901 (2015).

[5]M. Aspelmeyer, T. J. Kippenberg, and F. Marquardt, "Cavity optomechanics," Rev. Mod. Phys. **86**, 1391 (2014).

[6]W. L. Barnes, A. Dereux, and T. W. Ebbesen, "Surface plasmon subwavelength optics," Nature **424**, 824–830 (2003).

[7]A. Imamoglu, D. Awschalom, G. Burkard, D. P. DiVincenzo, D. Loss, M. Sherwin, and A. Small, "Quantum information processing using quantum dot spins and cavity QED," Phys. Rev. Lett. **83**, 4204 (1999).

[8]C. Monroe, "Quantum information processing with atoms and photons," Nature **416**, 238–246 (2002).

[9]J. Q. You and F. Nori, "Quantum information processing with superconducting qubits in a microwave field," Phys. Rev. B **68**, 064509 (2003).

[10]R. J. Thompson, G. Rempe, and H. J. Kimble, "Observation of normal-mode splitting for an atom in an optical cavity," Phys. Rev. Lett. **68**, 1132 (1992).

[11]A. Wallraff, D. Schuster, A. Blais, L. Frunzio, R. Huang, J. Majer, S. Kumar, S. Girvin, and R. Schoelkopf, "Strong coupling of a single photon to a superconducting qubit using circuit quantum electrodynamics," Nature **431**, 162–167 (2004).

[12]J. Bellessa, C. Bonnand, J. C. Plenet, and J. Mugnier, "Strong coupling between surface plasmons and excitons in an organic semiconductor," Phys. Rev. Lett. **93**, 036404 (2004).

[13]J. Kasprzak, M. Richard, S. Kundermann, A. Baas, P. Jeambrun, J. M. J. Keeling, F. M. Marchetti, M. H. Szymańska, R. André, J. L. Staehli, V. Savona, P. B. Littlewood, B. Deveaud, and L. S. Dang, "Bose-Einstein condensation of exciton polaritons," Nature **443**, 409–414 (2006).

[14]J. P. Reithmaier, G. Sek, A. Löffler, C. Hofmann, S. Kuhn, S. Reitzenstein, L. V. Keldysh, V. D. Kulakovskii, T. L. Reinecke, and A. Forchel, "Strong coupling in a single quantum dot-semiconductor microcavity system," Nature **432**, 197–200 (2004).

[15]T. Yoshie, A. Scherer, J. Hendrickson, G. Khitrova, H. M. Gibbs, G. Rupper, C. Ell, O. B. Shchekin, and D. G. Deppe, "Vacuum Rabi splitting with a single quantum dot in a photonic crystal nanocavity," Nature **432**, 200–203 (2004).

[16]Y. Kubo, F. R. Ong, P. Bertet, D. Vion, V. Jacques, D. Zheng, A. Dréau, J.-F. Roch, A. Auffeves, F. Jelezko, J. Wrachtrup, M. F. Barthe, P. Bergonzo, and D. Esteve, "Strong coupling of a spin ensemble to a superconducting resonator," Phys. Rev. Lett. **105**, 140502 (2010).

[17]Y. Tabuchi, S. Ishino, T. Ishikawa, R. Yamazaki, K. Usami, and Y. Nakamura, "Hybridizing ferromagnetic magnons and microwave photons in the quantum limit," Phys. Rev. Lett. **113**, 083603 (2014).

[18]X. Zhang, C. L. Zou, L. Jiang, and H. X. Tang, "Strongly coupled magnons and cavity microwave photons," Phys. Rev. Lett. **113**, 156401 (2014).

[19]M. Brune, F. Schmidt-Kaler, A. Maali, J. Dreyer, E. Hagley, J. M. Raimond, and S. Haroche, "Quantum Rabi oscillation: A direct test of field quantization in a cavity," Phys. Rev. Lett. **76**, 1800–1803 (1996).

[20]J. M. Raimond, M. Brune, and S. Haroche, "Manipulating quantum entanglement with atoms and photons in a cavity," Rev. Mod. Phys. **73**, 565–582 (2001).

[21]C. J. Hood, T. W. Lynn, A. C. Doherty, A. S. Parkins, and H. J. Kimble, "The atom-cavity microscope: Single atoms bound in orbit by single photons," Science **287**, 1447–1453 (2000).

[22]C. Weisbuch, M. Nishioka, A. Ishikawa, and Y. Arakawa, "Observation of the coupled exciton-photon mode splitting in a semiconductor quantum microcavity," Phys. Rev. Lett. **69**, 3314–3317 (1992).

[23]R. Ameling and H. Giessen, "Cavity plasmonics: Large normal mode splitting of electric and magnetic particle plasmons induced by a photonic microcavity," Nano Lett. **10**, 4394–4398 (2010).

[24]Y. S. Park, A. K. Cook, and H. Wang, "Cavity QED with diamond nanocrystals and silica microspheres," Nano Lett. **6**, 2075–2079 (2006).

[25]H. Huebl, C. W. Zollitsch, J. Lotze, F. Hocke, M. Greifenstein, A. Marx, R. Gross, and S. T. B. Goennenwein, "High cooperativity in coupled microwave resonator ferrimagnetic insulator hybrids," Phys. Rev. Lett. **111**, 127003 (2013).

[26]Q. Zhang, M. Lou, X. Li, J. L. Reno, W. Pan, J. D. Watson, M. J. Manfra, and J. Kono, "Collective non-perturbative coupling of 2D electrons with high-quality-factor terahertz cavity photons," Nat. Phys. **12**, 1005–1011 (2016).

[27]T. D. Ladd, F. Jelezko, R. Laflamme, Y. Nakamura, C. Monroe, and J. L. O'Brien, "Quantum computers," Nature **464**, 45–53 (2010).

[28]M. Brune, S. Haroche, J. M. Raimond, L. Davidovich, and N. Zagury, "Manipulation of photons in a cavity by dispersive atom-field coupling: Quantum-nondemolition measurements and generation of "Schrödinger cat" states," Phys. Rev. A **45**, 5193–5214 (1992).

[29]J. Q. You and F. Nori, "Atomic physics and quantum optics using superconducting circuits," Nature **474**, 589 (2011).

[30]A. V. Chumak, A. A. Serga, M. B. Jungfleisch, R. Neb, D. A. Bozhko, V. S. Tiberkevich, and B. Hillebrands, "Direct detection of magnon spin transport by the inverse spin Hall effect," Appl. Phys. Lett. **100**, 082405 (2012).

[31]Y. Kajiwara, K. Harii, S. Takahashi, J. Ohe, K. Uchida, M. Mizuguchi, H. Umezawa, H. Kawai, K. Ando, K. Takanashi, S. Maekawa, and E. Saitoh, "Transmission of electrical signals by spin-wave interconversion in a magnetic insulator," Nature **464**, 262–266 (2010).

[32]R. W. Sanders, V. Jaccarino, and S. M. Rezende, "Magnetic polariton, impurity mode enhancement, and superradiance effects in FeF$_2$," Solid State Commun. **28**, 907–910 (1978).

[33]T. Kampfrath, A. Sell, G. Klatt, A. Pashkin, S. Mährlein, T. Dekorsy, M. Wolf, M. Fiebig, A. Leitenstorfer, and R. Huber, "Coherent terahertz control of antiferromagnetic spin waves," Nat. Photon. **5**, 31–34 (2011).

[34]A. V. Kimel, A. Kirilyuk, P. A. Usachev, R. V. Pisarev, A. M. Balbashov, and T. Rasing, "Ultrafast non-thermal control of magnetization by instantaneous photomagnetic pulses," Nature **435**, 655–657 (2005).

[35]S. Baierl, M. Hohenleutner, T. Kampfrath, A. K. Zvezdin, A. V. Kimel, R. Huber, and R. V. Mikhaylovskiy, "Nonlinear spin control by terahertz-driven anisotropy fields," Nat. Photon. **10**, 715–718 (2016).

[36]T. F. Nova, A. Cartella, A. Cantaluppi, M. Först, D. Bossini, R. V. Mikhaylovskiy, A. V. Kimel, R. Merlin, and A. Cavalleri, "An effective magnetic field from optically driven phonons," Nat. Phys. **1**, 1–13 (2016).

[37]J. Lu, X. Li, H. Y. Hwang, B. K. Ofori-Okai, T. Kurihara, T. Suemoto, and K. A. Nelson, "Coherent two-dimensional terahertz magnetic resonance spectroscopy of collective spin waves," Phys. Rev. Lett. **118**, 207204 (2017).

[38]B. A. Ivanov, "Spin dynamics of antiferromagnets under action of femtosecond laser pulses (Review Article), " Low Temp. Phys. **40**, 91 (2014).

[39]D. Talbayev, S. A. Trugman, A. V. Balatsky, T. Kimura, A. J. Taylor, and R. D. Averitt, "Detection of coherent magnons via ultrafast pump-probe reflectance spectroscopy in multiferroic Ba$_{0.6}$Sr$_{1.4}$Zn$_2$Fe$_{12}$O$_{22}$," Phys. Rev. Lett. **101**, 097603 (2008).

[40]A. M. Kalashnikova, A. V. Kimel, R. V. Pisarev, V. N. Gridnev, A. Kirilyuk, and T. Rasing, "Impulsive generation of coherent magnons by linearly polarized light in the easy-plane antiferromagnet FeBO$_3$," Phys. Rev. Lett. **99**, 167205 (2007).

[41]K. Yamaguchi, M. Nakajima, and T. Suemoto, "Coherent control of spin precession motion with impulsive magnetic fields of half-cycle terahertz radiation," Phys. Rev. Lett. **105**, 237201 (2010).

[42]T. Feurer, J. C. Vaughan, and K. A. Nelson, "Spatiotemporal coherent control of lattice vibrational waves," Science **299**, 374–377 (2003).

[43]C. A. Werley, K. Fan, A. C. Strikwerda, S. M. Teo, X. Zhang, R. D. Averitt, and K. A. Nelson, "Time-resolved imaging of near-fields in THz antennas and direct quantitative measurement of field enhancements," Opt. Express **20**, 8551 (2012).

[44]P. Sivarajah, B. K. Ofori-Okai, S. M. Teo, C. A. Werley, and K. A. Nelson, "The homogenization limit and waveguide gradient index devices demonstrated through direct visualization of THz fields," New J. Phys. **17**, 013013 (2015).

[45]C. Fenfen, Y. Shujuan, W. Yabin, Z. Sheng, C. Shixun, W. Anhua, and X. Jun, "Growth and surface morphology of ErFeO$_3$ single crystal," J. Cryst. Growth **318**, 932–935 (2011).

[46]W. Yabin, C. Shixun, S. Mingjie, Y. Shujuan, K. Baojuan, Z. Jincang, W. Anhua, and X. Jun, "Growth rate dependence of the NdFeO$_3$ single crystal grown by float zone technique," J. Cryst. Growth **318**, 927–931 (2011).

[47]R. Huang, S. Cao, W. Ren, S. Zhan, B. Kang, and J. Zhang, "Large rotating field entropy change in ErFeO$_3$ single crystal with angular distribution contribution," Appl. Phys. Lett. **103**, 162412 (2013).

[48]E. Yablonovitch, "Inhibited spontaneous emission in solid-state physics and electronics," Phys. Rev. Lett. **58**, 2059–2062 (1987).

[49]S. John, "Strong localization of photons in certain disordered dielectric superlattices," Phys. Rev. Lett. **58**, 2486–2489 (1987).

[50]J. D. Joannopoulos, S. G. Johnson, J. N. Winn, and R. D. Meade, *Photonic Crystals Molding the Flow of Light*, 2nd ed. (Princeton University Press, Princeton, NJ, 2008), pp. 52–54.

[51]P. Sivarajah, C. A. Werley, B. K. Ofori-Okai, and K. A. Nelson, "Chemically assisted femtosecond laser machining for applications in LiNbO$_3$ and LiTaO$_3$," Appl. Phys. A **112**, 615–622 (2013).

[52]A. R. A. Chalcraft, S. Lam, D. O'Brien, T. F. Krauss, M. Sahin, D. Szymanski, D. Sanvitto, R. Oulton, M. S. Skolnick, A. M. Fox, D. M. Whittaker, H. Y. Liu, and M. Hopkinson, "Mode structure of the L3 photonic crystal cavity," Appl. Phys. Lett. **90**, 241117 (2007).

[53]T. Feurer, N. S. Stoyanov, D. W. Ward, J. C. Vaughan, E. R. Statz, and K. A. Nelson, "Terahertz polaritonics," Annu. Rev. Mater. Res. **37**, 317–350 (2007).

[54]S. M. Shapiro, J. D. Axe, and J. P. Remeika, "Neutron-scattering studies of spin waves in rare-earth orthoferrites," Phys. Rev. B **10**, 2014 (1974).

[55]T. Dougherty, G. Wiederrecht, and K. Nelson, "Impulsive stimulated Raman scattering experiments in the polariton regime," J. Opt. Soc. Am. B **9**, 2179–2189 (1992).

[56]K.-L. Yeh, M. C. Hoffmann, J. Hebling, and K. A. Nelson, "Generation of 10 μJ ultrashort terahertz pulses by optical rectification," Appl. Phys. Lett. **90**, 171121 (2007).

[57]C. Yang, Q. Wu, J. Xu, K. A. Nelson, and C. A. Werley, "Experimental and theoretical analysis of THz-frequency, direction-dependent, phonon polariton modes in a subwavelength, anisotropic slab waveguide," Opt. Express **18**, 26351–26364 (2010).

[58]C. Winnewisser, P. U. Jepsen, M. Schall, V. Schyja, and H. Helm, "Electro-optic detection of THz radiation in LiTaO$_3$, LiNbO$_3$ and ZnTe," Appl. Phys. Lett. **70**, 3069 (1997).

[59]I. P. Kaminow and W. D. Johnston, Jr., "Quantitative determination of sources of the electro-optic effect in LiNbO$_3$ and LiTaO$_3$," Phys. Rev. **160**, 519 (1967).

[60]G. V. Kozlov, S. P. Lebedev, A. A. Mukhin, A. S. Prokhorov, L. V. Fedorov, A. M. Balbashov, and I. Y. Parsegov, "Submillimeter backward-wave oscillator spectroscopy of the rare-earth orthoferrites," IEEE Trans. Magn. **29**, 3443–3445 (1993).

[61]Y. Zhu, D. J. Gauthier, S. E. Morin, Q. Wu, H. J. Carmichael, and T. W. Mossberg, "Vacuum Rabi splitting as a feature of linear-dispersion theory: Analysis and experimental observations," Phys. Rev. Lett. **64**, 2499 (1990).

[62]J. M. Fink, L. Steffen, P. Studer, L. S. Bishop, M. Baur, R. Bianchetti, D. Bozyigit, C. Lang, S. Filipp, P. J. Leek, and A. Wallraff, "Quantum-to-classical transition in cavity quantum electrodynamics," Phys. Rev. Lett. **105**, 163601 (2010).

[63]X. Li, M. Bamba, N. Yuan, Q. Zhang, Y. Zhao, M. Xiang, K. Xu, Z. Jin, W. Ren, G. Ma, S. Cao, D. Turchinovich, and J. Kono, "Observation of Dicke cooperativity in magnetic interactions," Science **361**, 794–797 (2018).

[64]Since we limit ourselves to the lower phonon-polariton branch, the phonon and photon excursions are in-phase. An avoided crossing and beating between upper and lower phonon-polariton branches would occur around the bare phonon frequency, which is far higher than our present frequency range.[42]

[65]Note that the space-time plot in Fig. 3(b), which was used for the eigenmode analysis, starts at approximately 0.5 mm into the hybrid structure in order to avoid significant decaying wave contributions.[53]

[66]J. Zhou, T. Koschny, and C. M. Soukoulis, "Magnetic and electric excitations in split ring resonators," Opt. Express **15**, 17881–17890 (2007).

[67]C. A. Werley, S. M. Teo, B. K. Ofori-Okai, P. Sivarajah, and K. A. Nelson, "High-resolution, low-noise imaging in THz polaritonics," IEEE Trans. Terahertz Sci. Technol. **3**, 239–247 (2013).

[68]K. Wong, *Properties of Lithium Niobate* (The Institution of Engineering and Technology, 2002), p. 432.

[69]A. Ridah, M. D. Fontana, and P. Bourson, "Temperature dependence of the raman modes in LiNbO$_3$ and mechanism of the phase transition," Phys. Rev. B **56**, 5967 (1997).

[70]T. Qiu and M. Maier, "Long-distance propagation and damping of low-frequency phonon polaritons in LiNbO$_3$," Phys. Rev. B **56**, R5717 (1997).

[71]H. J. Bakker, S. Hunsche, and H. Kurz, "Coherent phonon polaritons as probes of anharmonic phonons in ferroelectrics," Rev. Mod. Phys. **70**, 523 (1998).

[72]L. Palfalvi, J. Hebling, J. Kuhl, A. Peter, and K. Polgar, "Temperature dependence of the absorption and refraction of Mg-doped congruent and stoichiometric LiNbO$_3$ in the THz range," J. Appl. Phys. **97**, 3505 (2005).

[73]N. Hodgson and H. Weber, *Laser Resonators and Beam Propagation: Fundamentals, Advanced Concepts, Applications* (Springer, 2005), Vol. 108.

[74]A. M. Balbashov, G. V. Kozlov, A. A. Mukhin, and A. S. Prokhorov, *Submillimeter Spectroscopy of Antiferromagnetic Dielectrics. Rare-Earth Orthoferrites* (World Scientific Publishing Company Inc., 1995).

[75]A. Scherer, G. Khitrova, H. M. Gibbs, M. Kira, and S. W. Koch, "Vacuum Rabi splitting in semiconductors," Nat. Phys. **2**, 81 (2006).

[76]K.-L. Yeh, M. C. Hoffmann, J. Hebling, and K. A. Nelson, "Generation of $10\,\mu J$ ultrashort terahertz pulses by optical rectification," Appl. Phys. Lett. **90**, 171121 (2007).

[77]C. Winnewisser, P. U. Jepsen, M. Schall, V. Schyja, and H. Helm, "Electro-optic detection of THz radiation in LiTaO$_3$, LiNbO$_3$, and ZnTe, " Appl. Phys. Lett. **70**, 3069 (1997).

[78]Z. Chen, X. Zhou, C. A. Werley, and K. A. Nelson, "Generation of high power tunable multicycle teraherz pulses," Appl. Phys. Lett. **99**, 071102 (2011).

[79]Y. Cho and K. Yamanouchi, "Nonlinear, elastic, piezoelectric, electrostrictive, and dielectric constants of lithium niobate," J. Appl. Phys. **61**, 875–887 (1987).

[80]H. Choi, M. Heuck, and D. Englund, "Self-similar nanocavity design with ultrasmall mode volume for single-photon nonlinearities," Phys. Rev. Lett. **118**, 223605 (2017).

[81]C. Riek, D. V. Seletskiy, A. S. Moskalenko, J. F. Schmidt, P. Krauspe, S. Eckart, S. Eggert, G. Burkard, and A. Leitenstorfer, "Direct sampling of electric-field vacuum fluctuations," Science **350**, 420–423 (2015).

[82]A. S. Moskalenko, C. Riek, D. V. Seletskiy, G. Burkard, and A. Leitenstorfer, "Paraxial theory of direct electro-optic sampling of the quantum vacuum," Phys. Rev. Lett. **115**, 263601 (2015).

[83]C. Riek, P. Sulzer, M. Seeger, A. S. Moskalenko, G. Burkard, D. V. Seletskiy, and A. Leitenstorfer, "Subcycle quantum electrodynamics," Nature **541**, 376–379 (2017).

[84]Y. Sun, P. Wen, Y. Yoon, G. Liu, M. Steger, L. N. Pfeiffer, K. West, D. W. Snoke, and K. A. Nelson, "Bose-Einstein condensation of long-lifetime polaritons in thermal equilibrium," Phys. Rev. Lett. **118**, 016602 (2017).

[85]Y. Sun, Y. Yoon, M. Steger, G. Liu, L. N. Pfeiffer, K. West, D. W. Snoke, and K. A. Nelson, "Direct measurement of polariton-polariton interaction strength," Nat. Phys. **13**, 870–875 (2017).

[86]D. Englund, I. Fushman, and J. Vuckovic, "General recipe for designing photonic crystal cavities," Opt. Express **13**, 5961–5975 (2005).

[87]K. Huang, "On the interaction between the radiation field and ionic crystals," in *Proceedings of the Royal Society London A: Mathematical Physical and Engineering Sciences* (The Royal Society, 1951), Vol. 208, pp. 352–365.

[88]A. S. Barker and R. Loudon, "Dielectric properties and optical phonons in LiNbO$_3$," Phys. Rev. **158**, 433–445 (1967).